POLITECNICO DI TORINO
Repository ISTITUZIONALE

Influence of atomizing gas and pressure on the metallurgical characteristics and environmental performance of K340 tool steel powder produced by vacuum induction

Original
Influence of atomizing gas and pressure on the metallurgical characteristics and environmental performance of K340 tool steel powder produced by vacuum induction melting inert gas atomization / Kenevisi, M.S., Gobber, F.S., Pashaei, N., Priarone, P.C., Biamino, S., Ugues, D.. - In: JOURNAL OF MATERIALS RESEARCH AND TECHNOLOGY. - ISSN 2238-7854. - STAMPA. - 42:(2026), pp. 8898-8916. [10.1016/j.jmrt.2026.05.147]

Availability:
This version is available at: 11583/3017157 since: 2026-10-28T15:55:59Z

Publisher:
Elsevier Editora Ltda

Published
DOI:10.1016/j.jmrt.2026.05.147

Terms of use:

This article is made available under terms and conditions as specified in the corresponding bibliographic description in the repository

Publisher copyright

(Article begins on next page)

19 November 2026

Journal of Materials Research and Technology 42 (2026) 8898–8916

Contents lists available at ScienceDirect

Journal of Materials Research and Technology

journal homepage: www.elsevier.com/locate/jmrt

Influence of atomizing gas and pressure on the metallurgical characteristics and environmental performance of K340 tool steel powder produced by vacuum induction melting inert gas atomization

Mohammad Saleh Kenevisi [a,c], Federico Simone Gobber [a,c,d,*], Nazanin Pashaei [b], Paolo C. Priarone [b,c], Sara Biamino [a,c,d], Daniele Ugues [a,c,d]

[a] Politecnico di Torino, Department of Applied Science and Technology (DISAT), Viale Teresa Michel 5, 15121, Alessandria, Italy
[b] Politecnico di Torino, Department of Management and Production Engineering (DIGEP), Corso Duca Degli Abruzzi 24, 10129, Torino, Italy
[c] Interdepartmental Center IAM@PoliTo - Integrated Additive Manufacturing, Corso Duca Degli Abruzzi 24, 10129, Torino, Italy
[d] National Interuniversity Consortium of Materials Science and Technology (INSTM), Via Giusti 9, 50121, Firenze, Italy

ARTICLE INFO

Keywords:
Gas atomization
K340 tool steel
Additive manufacturing
Directed energy deposition
Recycling
Carbon footprint

ABSTRACT

K340 tool steel is widely used in dies and tooling applications requiring high wear resistance, toughness, and durability; however, its availability as powder feedstock for additive manufacturing remains limited. In this study, K340 powder was produced from industrial scrap by vacuum induction melting inert gas atomization, with the aim of assessing key metallurgical characteristics and the environmental benefits of scrap recovery and valorization. Argon and nitrogen were used as atomizing gases at pressures of 40 and 45 bar, and their effects on powder yield, particle size distribution, morphology, flowability, chemical composition, microstructure, and carbon footprint were systematically investigated. Powders in the 45–125 μm range, suitable for directed energy deposition (DED), represented 41.8–54.6% of the atomized material. Argon atomization promoted higher yields in this target fraction, whereas nitrogen atomization resulted in higher apparent density and improved flowability (Hall flow time as low as ~14.2 s), together with finer solidification microstructures, as indicated by secondary dendrite arm spacing values close to 1 μm in the finest powder fraction (20–45 μm). The chemical composition of the powders remained consistent with the starting K340 scrap, while nitrogen atomization led to measurable nitrogen uptake, particularly in coarser particles. A cradle-to-gate carbon footprint assessment was carried out by comparing scrap-based, typical-grade, and virgin-grade feedstock scenarios. Although atomizing gas and pressure had only a limited influence on batch-level emissions compared to feedstock-related contributions, which dominate the overall carbon footprint, normalization per kilogram of useable powder highlighted the critical role of process yield. The use of industrial scrap reduced the carbon footprint by up to approximately 80% compared with virgin-grade feedstock. Overall, the results demonstrate that vacuum induction melting inert gas atomization can produce DED-suitable K340 powder from recycled scrap, meeting the requirements for DED applications while providing substantial environmental benefits.

1. Introduction

In recent years, additive manufacturing (AM) has become an established industrial approach for producing components with complex geometries across a wide range of applications. In metal AM, feedstock can be supplied either in wire or powder form, depending on the selected process category. Among the available routes, powder-based technologies account for a major share of industrial metal AM applications, as they enable high geometrical accuracy and material flexibility. Powder bed fusion using a laser beam (PBF-LB/M, according to ISO/ASTM 52900:2022), powder bed fusion using an electron beam (PBF-EB), and directed energy deposition (DED) are currently the most widely adopted powder-based AM technologies [1,2]. In these processes, the performance and reliability are strongly governed by the characteristics of the metallic powder, which are in turn dictated by the adopted powder production method. To ensure satisfactory part quality, powders must exhibit a well-defined particle size distribution (PSD) and morphology, as these features directly affect powder flowability, packing density, and process stability [3].

* Corresponding author. Politecnico di Torino, Department of Applied Science and Technology (DISAT), Viale Teresa Michel 5, 15121, Alessandria, Italy.
E-mail address: federico.gobber@polito.it (F.S. Gobber).

https://doi.org/10.1016/j.jmrt.2026.05.147
Received 11 March 2026; Received in revised form 1 May 2026; Accepted 13 May 2026
Available online 14 May 2026
2238-7854/© 2026 The Authors. Published by Elsevier B.V. This is an open access article under the CC BY-NC-ND license (http://creativecommons.org/licenses/by-nc-nd/4.0/).

Nomenclature

BFE	Basic flowability energy (mJ)
CBD	Conditioned bulk density (g/cm^3)
CF	Carbon footprint (kgCO_2/kg or kgCO_2/batch)
D10	Particle diameter below which 10% of the cumulative particle volume is found (μm)
D50	Median particle diameter (μm)
D90	Particle diameter below which 90% of the cumulative particle volume is found (μm)
DED	Directed energy deposition
FRI	Flow rate index (−)
GA	Gas atomization
GMR	Gas-to-melt mass flow rate ratio (−)
GWP	Global warming potential
HR	Hausner ratio (−)
LCA	Life cycle assessment
LCI	Life cycle inventory
PEF	Product Environmental Footprint
PSD	Particle size distribution
SDAS	Secondary dendrite arm spacing, λ (μm)
SI	Stability index (−)
VIGA	Vacuum induction melting inert gas atomization
λ_x	X-ray wavelength (Å)
β	Full width at half maximum of diffraction peak (rad)
θ	Bragg angle (rad)
ε	Lattice microstrain (−)
R	Cooling rate (K/s)

To meet the strict requirements imposed on powders for metal AM, several production routes are currently available. Among these, gas atomization (GA), water atomization (WA), plasma atomization (PA), and the plasma rotating electrode process (PREP) represent the main industrial manufacturing methods [4,5]. The selection of a specific powder production route depends on multiple factors, including the processed material, production costs, achievable production rates, and the resulting powder characteristics [6]. Among the available techniques, GA is currently the predominant method for the production of metal powders for AM applications. It enables the manufacture of powders with high metallurgical quality and favorable morphological characteristics, while offering a good balance between production cost and throughput [4]. Owing to its versatility, GA has been successfully applied to a wide range of alloy systems, including aluminum alloys [7–9], steels [10–12], nickel-based superalloys [13], titanium alloys and intermetallics (e.g., Ti-6Al-4V [14], TiAl [15]), Nd-Fe-B [16], and copper-based alloys such as Cu-Cr-Nb [17].

Furthermore, gas atomization enables the production of powders over a wide range of PSDs [18]. This feature is particularly advantageous for AM applications, as different AM processes require powders with distinct PSD ranges. From a technological standpoint, the GA process begins with the melting of the metallic charge in the crucible of an induction furnace under vacuum conditions, where it is held for a defined time to ensure chemical and/or thermal homogeneity. The molten metal is typically superheated by approximately 75–150 °C above its liquidus temperature [19]. It is then discharged through a refractory nozzle and atomized by a high-pressure gas flow. Depending on the alloy system and process requirements, argon, helium, or nitrogen may be employed as the atomizing gas [19–21]. As the atomized droplets travel through the atomization chamber, they solidify and are subsequently collected in a hopper at the bottom of system. A schematic representation of the process is provided in Fig. 1.

Despite being an established industrial powder production route, gas atomization presents several challenges related to the quality of the resulting powder particles. One of the primary concerns is the formation of internal gas porosity, which originates from the entrapment of high-pressure atomizing gas within the molten droplets and can adversely affect the mechanical performance of additively manufactured components. In addition, the formation of satellites (small particles adhering to the surface of larger powder particles) detrimentally impacts powder packing density and flowability [13]. These powder characteristics are governed by the processing conditions adopted during atomization. Several parameters influence the properties of GA powders, including melt superheating, nozzle geometry, and the pressure, type, and flow rate of the atomizing gas. In addition, gas-to-melt ratio and thermophysical properties governing heat transfer and droplet cooling play a key role [19,22,23]. For instance, Li et al. [8] reported that the use of nozzles with smaller inner diameters promotes the formation of fine,

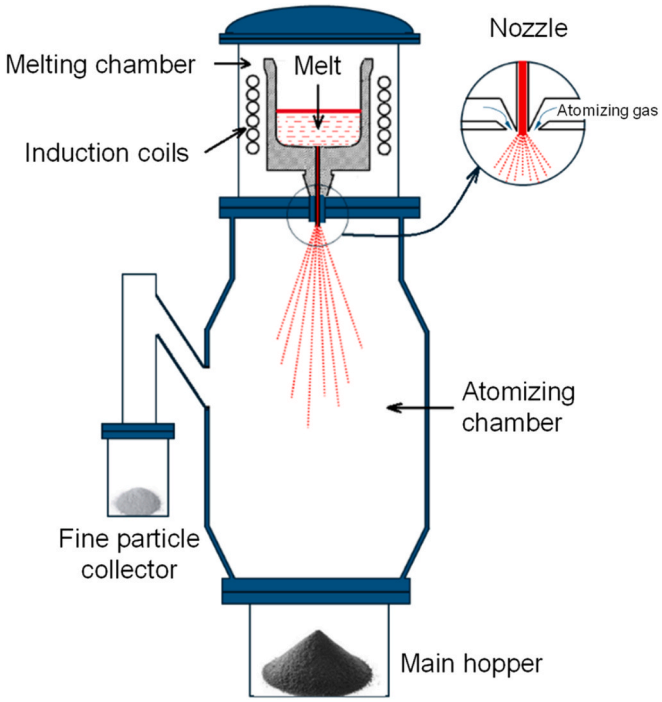


Fig. 1. Schematic representation of the gas atomization process.

spherical particles while reducing gas consumption. Similarly, an increase in melt superheat has been shown to lead to finer particle sizes, owing to the associated reduction in melt viscosity and surface tension [24].

Atomizing gas pressure represents another key process parameter governing powder particle characteristics. Increasing the gas pressure has been widely reported to reduce particle size; for instance, raising the pressure to 1.0 MPa was shown to decrease the mass median diameter of tin powders to approximately 23 μm, compared to 85 μm at 0.4 MPa [25], although the magnitude of this effect depends on the alloy system. Nevertheless, excessively high gas pressures may promote satellite formation and reduce particle sphericity, as demonstrated by combined computational fluid dynamics (CFD) and experimental studies by Wu et al. [13] and Cui et al. [22,26], ultimately leading to reduced powder flowability. Beyond particle size and morphology, atomizing gas pressure can also influence droplet cooling rates and, consequently, microstructural features of the solidified powders, including grain size and amorphous phase fraction, as reported for nanocrystalline soft magnetic composites [27]. More generally, the thermophysical properties of the

atomizing gas play a critical role in determining droplet cooling and solidification behavior, thereby affecting powder particle characteristics such as PSD and microstructure.

Argon and nitrogen are the most commonly employed atomizing gases and are widely recognized for their ability to limit oxidation during atomization. Owing to their different thermophysical properties, the use of these gases can lead to distinct solidification structures. In particular, argon is frequently preferred over nitrogen due to its higher chemical inertness, which has resulted in its widespread industrial adoption and extensive investigation in the literature [17,28,29]. However, recent research has increasingly focused on the use of nitrogen as an atomizing gas. While argon remains the most commonly employed option, nitrogen can offer distinct metallurgical and environmental advantages when used under appropriate processing conditions. Increased nitrogen content in steels has been reported to affect mechanical properties and corrosion resistance [30], as well as to promote the formation of a more homogeneous austenitic structure during hardening treatments in martensitic steels [31]. Furthermore, the addition of nitrogen to high-speed tool steels has been shown to enhance material toughness and resistance to adhesive wear [32]. In this context, recent studies on cryo-treated HSS tools and sound-based tool-wear classification have further highlighted that tool performance is governed not only by the intrinsic wear resistance of the tool material, but also by its thermal/-mechanical history and by the ability to monitor wear evolution during machining [33,34]. These findings emphasize the importance of wear-resistant tool steels and motivate the development of repair-oriented AM strategies. Beyond metallurgical considerations, from an environmental perspective, the substitution of argon with nitrogen as the atomizing gas (when technically feasible) has to be verified. Some studies report lower global warming potential (GWP) and cumulative energy demand (CED) of nitrogen compared with argon [35], although the magnitude of this advantage depends on the emission factors adopted for the industrial gases.

The metallurgical benefits of nitrogen are particularly relevant when considering high-performance materials. The influence of nitrogen addition on the hardness of high-carbon steels has been investigated by Hara et al. [36], who reported that alloys containing approximately 1000–1500 ppm nitrogen exhibit higher hardness values after quenching or tempering at relatively low or high temperatures, respectively, compared with nitrogen-free steels. This increase in hardness was attributed to an increased carbon content in the matrix, resulting from the partial substitution of carbon by nitrogen in carbide phases and the consequent release of carbon from carbides into the matrix. Nitrogen addition has been reported to promote solid-solution hardening and precipitation strengthening, while favoring the formation of fibrous M_2C carbides over M_6C and lamellar M_2C carbides [37–39]. Furthermore, nitrogen has been shown to reduce the average carbide size, which directly contributes to improved material toughness [40,41].

Such metallurgical refinement is particularly critical for tool steels, a class of materials designed to withstand extreme wear and mechanical loading in demanding industrial applications [42,43]. While tool steels are essential for the manufacture of cutting tools, molds, and dies, they are frequently subjected to wear, damage, or erosion, which can necessitate costly replacement. To address these challenges, additive manufacturing (AM) has been identified as a promising repair approach, offering significant cost savings by restoring damaged components with high precision and minimal material waste [44–46]. Using techniques such as directed energy deposition (DED) [47], a layer-by-layer restoration strategy enables precise control over the repair of high-value tools. However, the effectiveness of this approach is fundamentally constrained by the availability of suitable high-performance materials in powder form. Although K340 tool steel is highly regarded for the wear resistance and toughness required in these demanding applications [48,49], it is not currently available as a commercial powder feedstock, to the best of authors' knowledge.

In this context, the production of AM-grade powders for tool steels requires further research. In particular, when GA is employed to produce powders for demanding applications, a systematic evaluation of the role of key process parameters, such as atomizing gas type and pressure, is essential to ensure that the resulting powders meet both metallurgical and processing requirements. Moreover, by enabling the direct conversion of secondary feedstock into high-quality powder [50,51], vacuum induction melting inert gas atomization (VIGA) offers a promising pathway to support circular economy strategies in metal additive manufacturing. Accordingly, the objectives of this work are: (*i*) to demonstrate the feasibility of producing AM-grade K340 tool steel powder via VIGA using recycled industrial scrap as feedstock; (*ii*) to assess the influence of atomizing gas type and pressure on powder yield, particle size distribution, morphology, flowability, microstructure, and chemical composition; and (*iii*) to quantify the combined sustainability benefits arising from the use of recycled K340 scrap and alternative atomizing gases through a comparative LCA approach. This integrated strategy aims to reduce the environmental impact of powder production while preserving the metallurgical and physical properties required for AM applications. The study clarifies whether direct scrap atomization can provide a DED-suitable powder fraction while maintaining adequate physical, rheological, chemical, and microstructural characteristics. Furthermore, by comparing scrap-based, typical-grade, and virgin-grade feedstock scenarios, the work aims to identify the relative contribution of feedstock selection and atomization parameters to the overall environmental performance of K340 powder production. The experimental methodology and characterization procedures are described in Section 2, while the effects of atomizing gas and pressure on powder properties are discussed in Sections 3.1–3.7. The carbon footprint results and the role of feedstock strategy in powder decarbonization are then addressed in Section 3.8. Conclusions and outlook are summarized in Section 4.

2. Materials and methods

The raw material consisted of rolled K340 tool steel scrap, in the form of offcuts generated during the manufacturing of stamping dies, supplied by Util Industries S.p.A. The carbon content of the alloy was determined using a LECO CS844 analyzer, while the concentrations of the remaining alloying elements were measured by optical emission spectroscopy (OES) using a Metal LAB Plus equipment by GNR S.r.l. Three measurements were performed and averaged, and the resulting chemical composition of the material is reported in Table 1.

Prior to melting, the scrap was sectioned by band sawing to match the dimensions of the atomizer crucible and ultrasonically cleaned using acetone of commercial purity. Atomization was carried out using a Hermiga 100/10 VI gas atomizer (Phoenix Scientific Industries Limited). Prior to each atomization run, the melting chamber was evacuated to a pressure of 4×10^{-2} mbar. The material was then heated to 1600 °C, corresponding to a superheat of approximately 180 °C above the estimated liquidus temperature, and held at this temperature for 15 min. To facilitate the melt flow through the nozzle, an argon overpressure of 0.25 barg was applied to the melt. In addition, before atomization, the melt delivery nozzle (having an inner diameter of 2.4 mm) was resistively heated to prevent premature solidification of the melt during its discharge through the nozzle. In this study, the atomizing gas type and gas pressure were both varied. Argon and nitrogen were employed as atomizing gases, and atomization was carried out at gas pressures of either 40 or 45 bar. This relatively narrow pressure range was selected based on previous trials on super duplex stainless steels [52], where it was found to maximize the powder yield within the PSD suitable for DED, and was therefore adopted here as a practical operating window. Consequently, four different powder batches were produced (as summarized in Table 2) for subsequent characterization and environmental impact assessment, following the experimental procedure outlined in Fig. 2. The atomization process for each batch was completed within approximately 4 min.

Table 1
Chemical composition (wt.%) of the tool steel scrap for gas atomization (carbon was analyzed via combustion analysis and the remaining were measured by OES analysis).

Element	C	Cr	Mo	V	Si	Mn	Nb	Al	Fe
K340 bulk	1.06 ± 0.01	7.98 ± 0.02	2.05 ± 0.02	0.45 ± 0.01	0.74 ± 0.02	0.38 ± 0.01	0.11 ± 0.01	0.92 ± 0.01	balance

Table 2
The details of atomizing gas and pressure used for each batch of atomization.

Batch	Ar – 40 bar	Ar – 45 bar	N_2 – 40 bar	N_2 – 45 bar
Atomizing gas	Argon (Ar)	Argon (Ar)	Nitrogen (N_2)	Nitrogen (N_2)
Atomizing pressure (bar)	40	45	40	45

2.1. Powder characterization

After collection from the main hopper, powders from each atomization batch were characterized using a combination of particle size, chemical, physical, and microstructural analyses. All powder handling, sieving, and characterization activities were carried out under standard laboratory conditions, at an ambient temperature of approximately 20 °C and a relative humidity in the range of 45–55%. These conditions were maintained throughout the experimental campaign to limit the influence of environmental variations on powder flowability and handling. As a preliminary step, the powders were first sieved using a 250 μm mesh to remove gas-atomization debris (splats). The particle size distribution (PSD) of the cleaned powders was then measured using a Malvern Panalytical Mastersizer 3000 laser diffraction particle size analyzer. For further characterization, each powder batch was subsequently sieved and classified into five particle size ranges: (*i*) 20–45, (*ii*) 45–63, (*iii*) 63–106, (*iv*) 106–125, and (*v*) 125–250 μm. The chemical composition and alloying element contents of each size fraction were analyzed by scanning electron microscopy (SEM) coupled with energy-dispersive X-ray spectroscopy (EDS), using a Zeiss EVO 15 microscope equipped with an Ultim Max detector (Oxford Instruments). EDS quantification was performed at 20 kV and a working distance of 8.5 mm, using standards-based quantification. The contents of carbon, oxygen, and nitrogen were determined out of three measurement repetitions using LECO ONH836 and CS844 analyzers, employing inert gas fusion and combustion techniques, respectively. In addition to the previous powder size intervals a representative, homogenized sample of the 45–125 μm powder from each run was collected for N and O analysis. Particle morphology and shape descriptors were characterized using a Malvern Panalytical Morphologi 4 system, complementing the PSD data obtained by laser diffraction. Powder and bulk alloy densities were measured using an Ultrapyc 5000 gas pycnometer (Anton Paar), enabling the determination of relative density. Powder flowability was evaluated using an FT4 powder rheometer (Freeman Technology) and a Hall flowmeter funnel, in accordance with ASTM B213 [53]. Dry powder samples were used for both the rheological and the flowability tests (25 ml and 50 g, respectively). Powders were discarded after each test repetition. The experimental methods employed for rheological measurements are the same adopted by the authors in Ref. [54]. Microstructural characterization of the powders was performed using light optical microscopy (LOM) with a Leica DMI 5000 M microscope, SEM coupled with EDS, and X-ray diffraction (XRD) using a Panalytical Empyrean diffractometer.

To estimate the cooling rates of the atomized particles, a quantitative microstructural analysis was conducted by measuring the secondary dendrite arm spacing (SDAS) on polished powder cross-sections. Backscattered electron (BSE) micrographs acquired by SEM were analyzed using image analysis software (ImageJ), owing to the enhanced contrast between dendritic features. For each particle size range (20–45, 45–63, 63–106, 106–125, and 125–250 μm), a minimum of five particles was examined, with at least three independent SDAS measurements performed per particle. SDAS values were determined using the line-

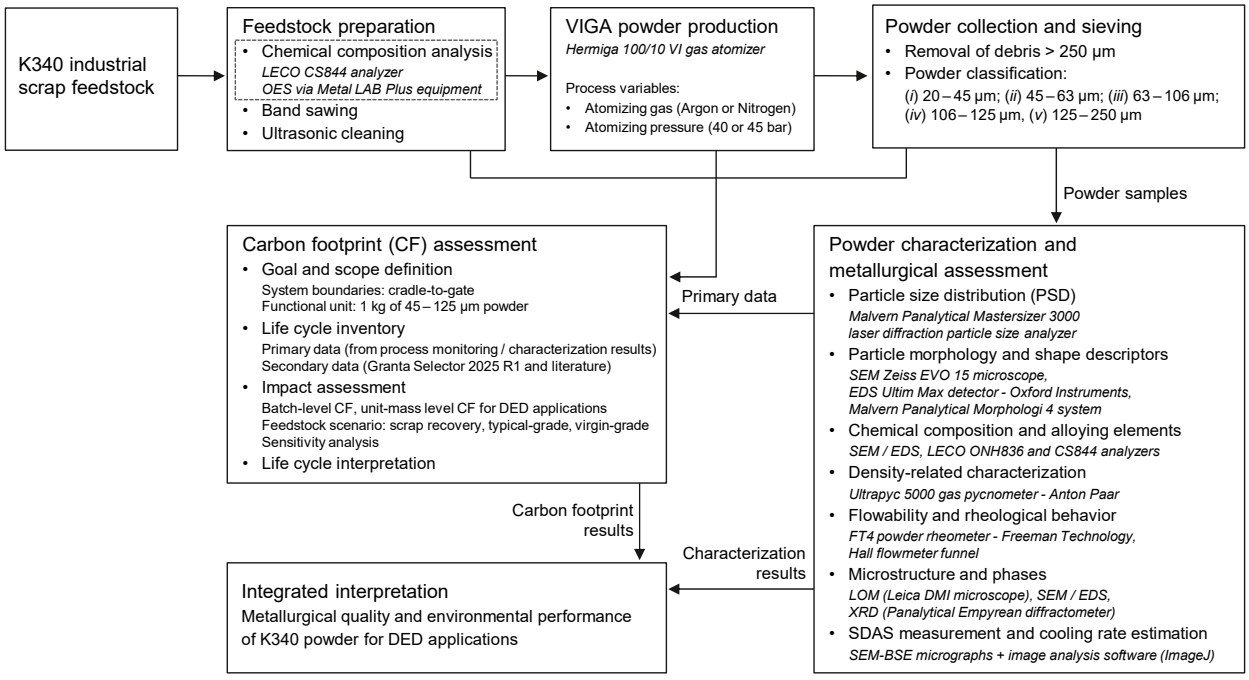


Fig. 2. Flowchart illustrating the integrated methodological approach adopted in this study, combining K340 powder production via VIGA, powder characterization, and carbon footprint assessment.

intercept method, as expressed by Eq. (1):

$$\lambda = \frac{L}{n_{arms} - 1} \quad (1)$$

where L represents the total length of a line traced across multiple adjacent secondary dendrite arms in the micrograph, while n_{arms} denotes the number of dendrite arms intersected by the line. Measurements were performed on randomly oriented line segments to minimize directional bias. The resulting value corresponds to the secondary dendrite arm spacing, λ, expressed in micrometers (μm).

Subsequently, empirical correlations reported in the literature were employed to estimate the cooling rates of the solidifying droplets from the experimentally measured SDAS values. Dendrite arm spacing is widely recognized to exhibit an inverse dependence on the cooling rate, commonly described by a power-law relationship. In this context, Jegede et al. [55] demonstrated that cooling rates during gas atomization can be estimated by correlating SDAS with the solidification rate. The general form of this relationship is expressed in Eq. (2):

$$\lambda = A \cdot R^{-n} \quad (2)$$

where R denotes the cooling rate, while A and n are material-specific constants. As no specific correlation has been reported for Böhler K340 steel, an established relationship developed for a comparable tool steel was adopted. Specifically, Mao et al. [56] proposed a calibration for AISI H13 steel that relates the local cooling rate to the secondary dendrite arm spacing, as reported in Eq. (3):

$$\lambda = 175.4 \cdot R^{-0.322} \quad (3)$$

In this formulation, R is expressed in units of °C/min. The correlation derived for H13 steel was employed to estimate the cooling rates of K340 powder particles based on the experimentally measured SDAS values, under the assumption of comparable solidification behavior of the molten alloys. Nevertheless, differences in chemical composition between H13 and K340 steels may influence the quantitative relationship between SDAS and cooling rate; therefore, the resulting cooling rate values should be regarded as approximate. Accordingly, the estimated cooling rates were primarily used for comparative analysis of the solidification conditions associated with argon and nitrogen atomization.

2.2. Carbon footprint assessment

The carbon footprint assessment was conducted in accordance with Life Cycle Assessment (LCA) principles, following the requirements of ISO 14040, ISO 14044, and ISO 14067 [57–59], and in alignment with the methodological guidance of the Product Environmental Footprint (PEF) framework proposed by the Joint Research Centre of the European Commission [60]. The primary objective of the assessment was to quantify and compare the carbon footprint of gas-atomized K340 steel powders produced under different atomization conditions, specifically varying the atomizing gas type and pressure, as well as the origin of the feedstock material. Three distinct feedstock categories were considered: (*i*) the pre-consumer recycled content in the form of bulky industrial scrap, (*ii*) a commercially supplied typical-grade material, representative of average market-grade steel production and inherently containing a background level of recycled content, and (*iii*) a virgin-grade material, with no benefits related to material recycling. The latter two scenarios were included to quantify the potential benefits of direct scrap atomization in view of powder decarbonization [61].

A cradle-to-gate system boundary was adopted, and carbon dioxide equivalent emissions were selected as the environmental impact indicator. A functional unit of 1 kg of AM powder within the 45–125 μm particle size range, representative of Directed Energy Deposition (DED) applications, was defined. Accordingly, the system boundary encompassed raw material production, feedstock or scrap preparation, gas atomization, and final sieving. In accordance with the PEF methodology, a recycled content modelling approach (100:0) was applied to the pre-consumer scrap scenario, whereby secondary material inputs were assigned only the environmental impacts associated with preparation processes, while no upstream burdens from primary raw material extraction and processing were allocated. Conversely, typical-grade materials were modelled using background datasets representative of average market supply, in which recycled content (if any) is already embedded and accounted for within the upstream life cycle inventory. To evaluate the influence of powder feedstock on the overall environmental performance of additively manufactured components, the carbon footprint of powder production was contextualized against representative literature values for DED processes. This comparison provides an indication of whether the carbon footprint of the final component is predominantly driven by material-related aspects when different powder feedstocks are employed.

In line with PEF recommendations for cradle-to-gate studies of intermediate products [59,60], the other downstream phases were excluded from the analysis. Furthermore, capital goods (e.g., atomization machinery and infrastructure), packaging, and transportation activities were excluded from the assessment, as they were assumed to be either negligible or identical across scenarios and not discriminatory for the comparative purpose of the study. Fig. 3 schematically illustrates the adopted system boundaries and the integrated assessment framework.

3. Results and discussion

3.1. Process efficiency and yield factors

Gas atomization typically produces powders with a wide PSD, ranging from submicrometric particles to coarse particles approaching 300 μm. The atomizer used in this study was equipped with two collection hoppers: a main hopper, in which most of the powder was collected, and a secondary hopper, where fine particles remaining suspended in the exhaust gas were recovered following cyclone separation. The fine fraction collected in the secondary hopper was not considered suitable for DED applications and was therefore excluded from further characterization. Nevertheless, the powder mass collected in both hoppers was measured in order to determine the overall powder yield relative to the initial charged mass.

The distribution of powder yields across the investigated atomization parameters is summarized in Table 3. The results indicate that the powder yield within the 45–125 μm particle size range, suitable for the DED process, varied between 41.8 and 54.6 % across all batches. Notably, nitrogen-atomized powders exhibited a comparatively lower yield within the target size range than argon-atomized batches. This difference is attributed to the thermophysical properties of the atomizing gases, as the higher cooling rate provided by nitrogen likely promoted the formation of a thin solidified layer adhering to the atomizing nozzle (as further discussed in the following sections), which can be described as an incipient melt freezing at the nozzle. The presence of this layer altered the effective gas-melt interaction and shifted the particle size distribution toward coarser fractions (>125 μm) in the nitrogen batches. Under these conditions, increases in argon pressure were associated with further particle size refinement, while the nitrogen runs were limited by nozzle solidification effects.

3.2. Morphological characterization

SEM micrographs of the powder particles are presented in Fig. 4. The particles exhibit predominantly spherical morphology with a limited fraction of attached satellites. No significant differences in overall particle morphology were observed between the batches, although subtle variations in satellite content and particle contour were identified. Based on the literature, a higher fraction of satellite particles is likely to be observed in argon-atomized powders, whereas nitrogen-atomized

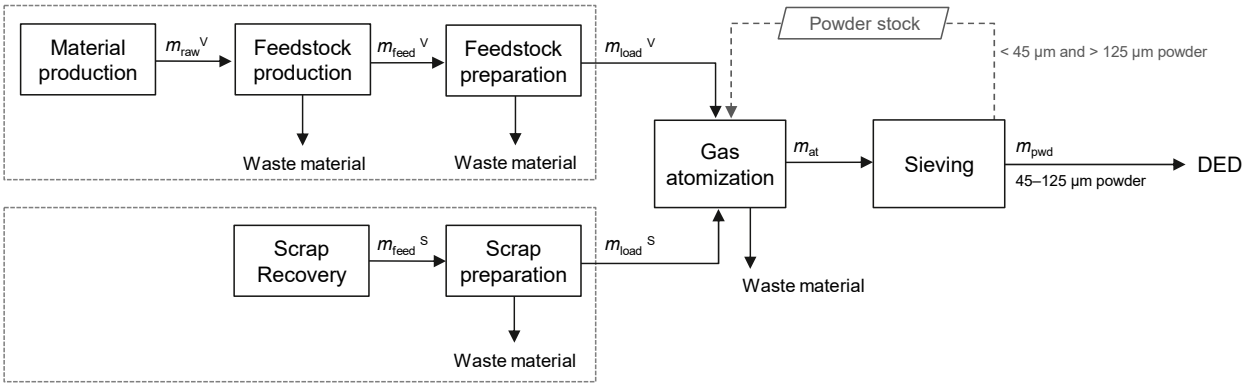


Fig. 3. System boundaries adopted for the carbon footprint assessment, highlighting the two alternative material input streams considered for powder production.

Table 3
Powder yield as a function of atomizing gas type and pressure.

Batch	Ar – 40 bar	Ar – 45 bar	N_2 – 40 bar	N_2 – 45 bar
<20 µm-size yield (wt.%)	2.1	4.0	1.9	1.4
20–45 µm-size yield (wt. %)	12.2	16.2	11.0	9.7
45–125 µm-size yield (wt. %)	50.8	54.6	43.3	41.8
>125 µm-size yield (wt.%)	34.9	25.2	43.8	47.1

powders should have a greater occurrence of irregularly shaped particles. The possibility of increased satellite formation under argon conditions can be attributed to comparatively lower cooling rates, which maintain the droplets in a semi-molten state for a longer duration. This allows smaller particles to adhere to the surface of larger droplets upon collision within the atomization chamber. In contrast, the higher cooling rates associated with nitrogen atomization lead to faster solidification, thereby limiting the time available for spheroidization and potentially promoting the formation of slightly more irregular particle shapes. While it has been reported that argon atomization tends to produce powders with higher sphericity and lower surface roughness, the qualitative analysis of Fig. 4 suggests that this advantage is relatively limited in this experimental study, and partially offset by the satellite content.

More specifically, Fig. 4a (Ar – 40 bar) and Fig. 4b (Ar – 45 bar) show particles with slightly smoother and more regular outlines than Fig. 4c (N_2 – 40 bar) and Fig. 4d (N_2 – 45 bar), but they also exhibit a slightly higher frequency of fine adhered satellites, so the overall morphological advantage remains limited. In the nitrogen-atomized powders, the fraction of attached satellites appears marginally reduced, although the particle contours are somewhat less relaxed and locally more irregular. Raising the atomizing pressure from 40 to 45 bar produces only subtle changes in both gas series: global sphericity remains high, and the main visible effect is a small variation in the population of fine secondary particles and surface attachments rather than a marked improvement in particle roundness. This behavior is consistent with the combined thermal and fluid dynamic action of the atomizing conditions. Under otherwise comparable conditions, Ar is expected to keep droplets deformable for slightly longer, favoring surface tension-driven spheroidization, whereas N_2 promotes earlier solidification and therefore slightly limits final shape spheroidization. At the same time, higher

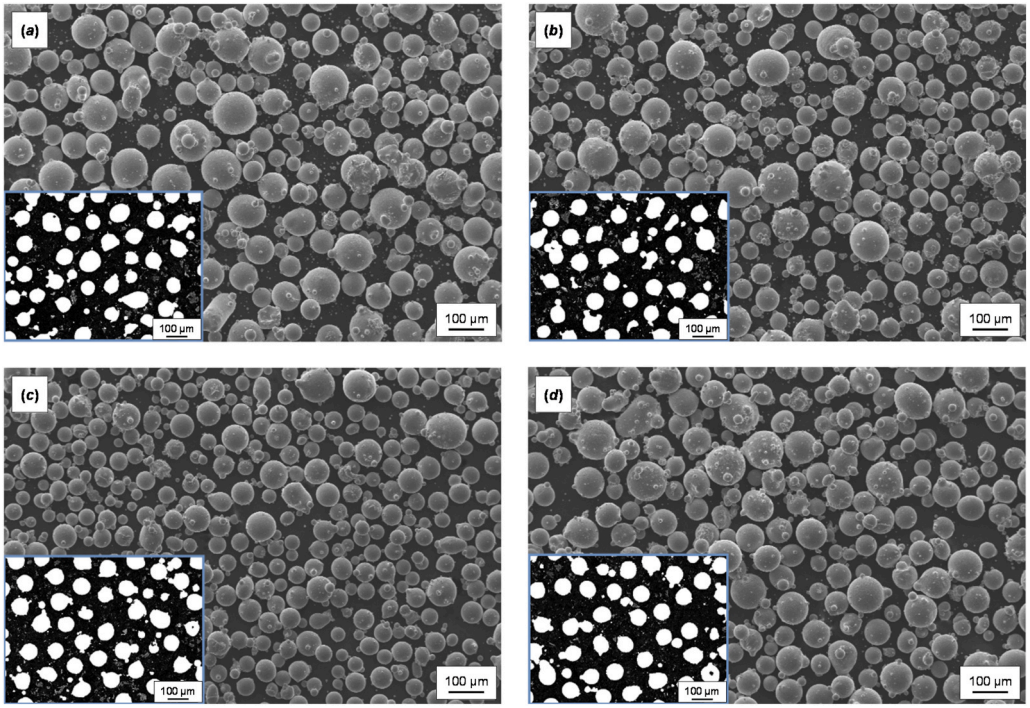


Fig. 4. SEM micrographs of powder particles atomized by (*a*) Ar–40 bar, (*b*) Ar–45 bar, (*c*) N_2–40 bar, and (*d*) N_2–45 bar.

pressure enhances gas-melt momentum exchange and secondary breakup, and can increase the population of fine droplets that collide with larger still-semi-molten particles and remain attached as satellites [62,63].

PSD analysis was carried out on the collected powders after the removal of very fine particles and splats by sieving, and the corresponding results are reported in Fig. 5 and Table 4. Analysis of the as-atomized state reveals a notable shift in the PSD of nitrogen-atomized powders toward coarser values compared to their argon-atomized counterparts. This observation deviates from established literature trends [64,65], which suggest that nitrogen atomization typically yields finer particles due to nitrogen absorption reducing the surface tension of the melt. As previously noted in the yield analysis, this unexpected coarsening is attributed to the incipient freezing at the melt delivery nozzle, which reduced the effectiveness of the atomizing gas in fragmenting the molten stream into finer droplets by physically hindering the gas-melt interaction.

This observed shift toward coarser diameters in the nitrogen batches is further emphasized when examining the effect of gas pressure. In the argon-atomized runs, increasing the gas pressure from 40 to 45 bar followed standard atomization behavior, successfully refining the D50 from 93 μm to 81 μm. This trend is consistent with established experimental studies [66] and numerical simulations [67], suggesting that higher atomizing pressures generally promote smaller median particle diameters. In contrast, the nitrogen-atomized powders showed an increase in the D50 from 112 μm to 118 μm as the atomization gas pressure was increased to 45 bar. This is associated with the enhanced cooling effect at the nozzle under higher nitrogen pressures, which promoted further accumulation of the solidified material layer. Consequently, instead of promoting finer droplets, the increased pressure further shielded the molten stream from effective fragmentation. These results emphasize that, for the gas atomizer configuration adopted in this study, the thermophysical impact of nitrogen on nozzle stability appears to be a more dominant factor in determining final particle size than the theoretical reduction in surface tension.

These observed trends are supported by the Gas-to-Melt mass flow rate Ratio (GMR) values presented in Table 5, which serves as a critical parameter for describing the relative intensity of gas-melt interaction during the atomization process. Theoretically, a higher GMR enhances the interaction between the gas and the molten stream, resulting in a more efficient fragmentation that shifts the PSD toward finer fractions. As summarized in Table 5, the argon-atomized batches yielded consistently higher GMR values compared to the nitrogen runs, correlating with the lower D50 values observed in the argon-atomized powder. Specifically, increasing the argon pressure from 40 to 45 bar raised the

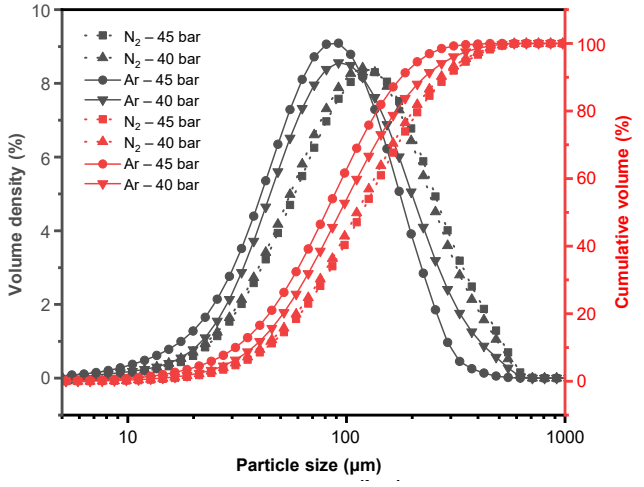


Fig. 5. PSD of argon- and nitrogen-atomized powders with different pressures.

Table 4
PSD of powders atomized using argon and nitrogen at different pressures in the as-atomized condition.

Batch	Ar – 40 bar	Ar – 45 bar	N_2 – 40 bar	N_2 – 45 bar
D10 (μm)	37	31	41	43
D50 (μm)	93	81	112	118
D90 (μm)	228	179	270	287

Table 5
GMR values of different batches of atomization.

Batch	Ar – 40 bar	Ar – 45 bar	N_2 – 40 bar	N_2 – 45 bar
GMR	1.49	1.53	1.15	1.40

GMR from 1.49 to 1.53, contributing to the successful refinement of the particle size. In contrast, the nitrogen-atomized batches exhibited lower GMR values, ranging from 1.15 to 1.40. While literature regarding A2 tool steel indicates that the GMR can increase three to five times when atomizing pressure is doubled [10], the variations in this study were less pronounced due to the relatively narrow pressure increment employed. Nevertheless, the data suggests that the occurrence of the previously discussed incipient freezing during nitrogen atomization likely reduced the overall gas flow, effectively suppressing the GMR. This reduction in available fragmentation energy provides a quantitative indication for the coarser powders obtained in the nitrogen batches, further demonstrating that the thermophysical impact of the gas on nozzle stability is a key factor governing process efficiency in this system.

A plausible explanation for the occurrence of melt incipient freezing at the delivery nozzle is that recirculation at the melt delivery nozzle tip draws melt onto the outer nozzle lip (a phenomenon known as *lick-back*), where expansion cooling rapidly solidifies it [68]. N_2 can plausibly trigger freezing where Ar does not, because of the higher droplet cooling rates with N_2 than Ar, so any melt touching the colder lip will form a solid skin faster [69]. Second, nitrogen is not fully inert for steels: nitrogen uptake during melting/atomization has been demonstrated, and in Cr-rich steels local supersaturation at a colder lip could assist the formation of a solid deposit. Still, studies on bulk samples indicate that nitrogen is often mainly dissolved rather than precipitated, so for K340 this remains a secondary hypothesis [11].

Following the initial characterization, the focus was shifted toward evaluating the suitability of the powders for DED applications. For this purpose, the fractions corresponding to the 45–125 μm range were analyzed as a specific subset of the previously established five-range classification. The resulting PSD data for this DED-specific classification are summarized in Table 6. When considering the powder fraction intended for DED applications, the differences between the two atomizing gases become less pronounced.

To further characterize the suitability of the sieved fractions for DED applications, the morphological properties of the 45–125 μm subset were evaluated. While the classification process partially harmonized the PSD, the influence of the atomizing gas on the physical shape of the particles remains a critical factor for powder flowability and deposition behavior. Consequently, the circularity and aspect ratio of the particles within this specific range were investigated for each batch. For both parameters, a value approaching the maximum of 1.0 indicates a perfectly spherical geometry. The quantitative results of this analysis are

Table 6
PSD of powders atomized using argon and nitrogen at different pressures within the range of 45–125 μm.

Batch	Ar – 40 bar	Ar – 45 bar	N_2 – 40 bar	N_2 – 45 bar
D10 (μm)	48	47	50	49
D50 (μm)	77	76	79	77
D90 (μm)	121	121	123	119

detailed in Fig. 6 and Table 7.

In agreement with previous studies on gas-atomized stainless-steel feedstocks, argon atomization can promote slightly more regular particle morphologies than nitrogen atomization, although the magnitude of this effect is often limited and not always fully captured by conventional shape descriptors alone [62]. In the present study, this tendency is visible but modest: the particles produced in argon (Fig. 4a and b) exhibit marginally smoother and more regular outlines than those produced in nitrogen (Fig. 4c and d), yet the differences in aspect ratio and circularity reported in Table 7 remain small. Moreover, circularity is generally expected to decrease with increasing particle size, in accordance with the literature [30]. This behavior can be rationalized by the higher probability of collision-induced deformation and satellite attachment in larger droplets, which remain partially liquid for longer and therefore interact more readily with recirculated fine particles during flight [63]. Consequently, the qualitative analysis of Fig. 4 and the quantitative data in Table 7 indicate that the argon-related advantage in particle regularity is present, but limited in the investigated 45–125 μm fraction. The cumulative impact of these morphological features extends to the macroscopic properties of the powder, as reflected in the density measurements provided in Table 8. Within the 45−125 μm range, the nitrogen-atomized powders exhibited consistently higher apparent and conditioned bulk densities compared to their argon-atomized counterparts. This observation contrasts with the shape factor analysis, where argon powders showed slightly higher sphericity. It suggests that the presence of satellites may play a more significant role in determining bulk density than the primary particle shape under the conditions investigated. Cleaner surfaces could facilitate a denser arrangement, whereas abundant satellites likely introduce inter-particle friction and void space, effectively reducing the overall density.

To provide a more comprehensive assessment of these density comparisons, the powders were subjected to a conditioning cycle. Conditioned bulk density (CBD) represents the density of the powder after it has been subjected to a specific, repeatable conditioning cycle designed to remove unstable air pockets, break up agglomerates, and establish a uniform, loosely defined state. The relative increase in density from the initial to the conditioned state, defined as the compressibility index, ranged between 5.7% and 6.2% across the four batches. A more critical indicator of rheological behavior is the Hausner Ratio (HR), calculated as the ratio of tapped density to bulk density. The HR serves as a standard metric for inter-particle friction. Generally, a compressibility index lower than 15% and a Hausner Ratio below 1.18 are indicative of excellent flowability [70–72]. As shown in Table 8, the nitrogen-atomized powders exhibited improved flow characteristics, achieving Hausner Ratios of 1.05 and 1.06, compared to 1.13 and 1.15 for the argon-atomized batches. This distinction reinforces the earlier morphological observations: the cleaner surfaces of the nitrogen-atomized particles minimize inter-particle friction, allowing for superior flowability.

To validate the static flow indications provided by the Hausner Ratio and compressibility index, the dynamic rheological behavior of the powders was assessed using Hall flowmeter and shear cell analysis, with results detailed in Table 9. The Hall flowability test was consistent with the trends observed in the density measurements; the nitrogen-atomized powders exhibited faster flow rates, requiring approximately 14 s to pass through the funnel compared to nearly 16 s for the argon-atomized batches. This behavior aligns with the fundamental principle that Hall flowability is highly affected by particle size and PSD, as larger particles tend to flow more freely due to lower surface area-to-volume ratios [73].

Complementing the Hall test, shear cell analysis provided a more granular evaluation of the powder response to dynamic stress through the Basic Flowability Energy (BFE). This parameter measures the energy required for the rheometer blade to move downward at a constant rotational speed during the seventh test cycle. Since BFE reflects the resistance encountered by the blade while passing through the powder, it is primarily influenced by the consolidation state and compressibility [74]. A lower BFE indicates that the powder yields easily to the blade, while a higher BFE suggests strong internal resistance. The rheological data is consistent with the Hall flowability results. Among the nitrogen-atomized batches, the powder produced at 40 bar, which exhibited the fastest Hall flow, correspondingly required the lowest BFE (424 mJ). Conversely, among the argon-atomized batches, the powder produced at 45 bar, which had the poorest Hall flowability, exhibited a marked increase in BFE (513 mJ).

Beyond the absolute magnitude of flow energy defined by the BFE, the temporal consistency of the feedstock was evaluated using the Stability Index (SI). This parameter is defined as the ratio between the downward flow energy measured during the seventh and first test cycles, and it reflects variations in powder flow behavior over time due to phenomena such as agglomeration, aeration, or electrostatic charging [75]. An SI value approaching 1.0 characterizes a stable, non-friable powder. As summarized in Table 9, all atomized batches displayed SI values tightly clustered between 0.98 and 1.02. This uniformity demonstrates that, despite the previously noted differences in inter-particle friction and morphology, all powders maintain consistent flow properties under cyclic mechanical stress. Consequently, the feedstock is unlikely to suffer from segregation during the prolonged handling sequences inherent to the DED process.

Finally, the sensitivity of the feedstock to changes in deformation rate was evaluated using the Flow Rate Index (FRI). While the SI assesses consistency over time, the FRI determines how the powder behaves under varying processing speeds. Specifically, this parameter is

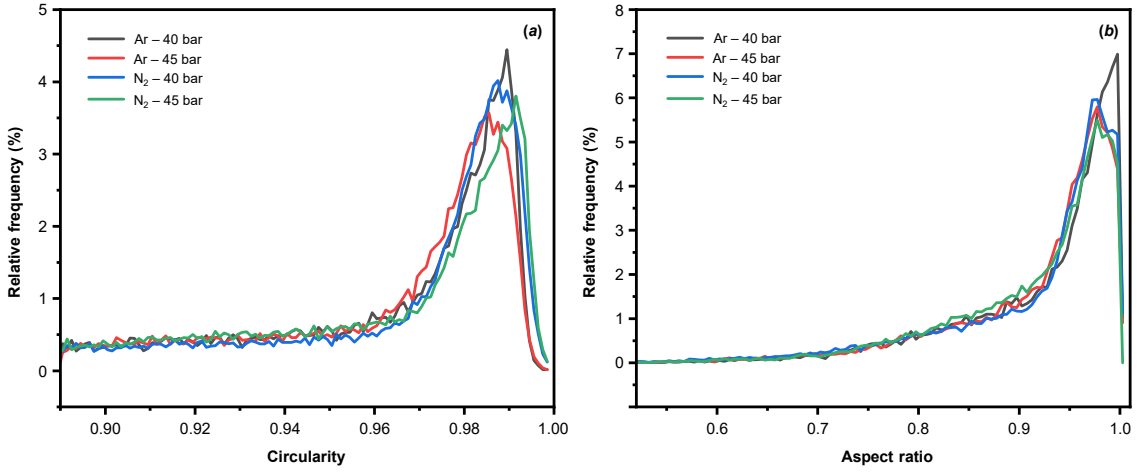


Fig. 6. Morphological characterization of the powders: (*a*) circularity and (*b*) aspect ratio.

Table 7
Circularity and aspect ratio of powders atomized using argon and nitrogen at different pressures.

Batch	Aspect Ratio				Circularity			
	D10	D50	D90	Mean	D10	D50	D90	Mean
Ar – 40 bar	0.801	0.953	0.992	0.922	0.916	0.976	0.989	0.965
Ar – 45 bar	0.799	0.948	0.988	0.919	0.915	0.975	0.988	0.964
N_2 – 40 bar	0.785	0.950	0.989	0.916	0.905	0.978	0.990	0.963
N_2 – 45 bar	0.796	0.943	0.989	0.915	0.909	0.975	0.991	0.962

Table 8
Density measurement of powders atomized using argon and nitrogen at different pressures.

Batch	Ar – 40 bar	Ar – 45 bar	N_2 – 40 bar	N_2 – 45 bar
Bulk (apparent) density (g/cm^3)	4.21	4.06	4.30	4.33
Conditioned bulk density (g/cm^3)	4.45	4.31	4.55	4.60
Tapped density (g/cm^3)	4.79	4.67	4.54	4.62
Hausner ratio (−)	1.13	1.15	1.05	1.06

Table 9
Powder flow properties obtained from hall funnel and shear cell rheometer for all the batches within the particle size range of 45–125 μm.

Batch	Ar – 40 bar	Ar – 45 bar	N_2 – 40 bar	N_2 – 45 bar
Hall flowability (s)	15.7	16.4	14.2	14.5
Basic flowability energy (mJ)	447	513	424	524
Stability index	1.02	1.01	0.98	1.00
Flow rate index	1.02	1.06	1.04	1.02

calculated by comparing the downward flow energy of the final test cycle (blade rotating at 20 mm/min) to that of the eighth test cycle (blade rotating at 100 mm/min). Typically, FRI values exceed 1, as powders tend to flow more easily at higher blade speeds [76]. However, an FRI surpassing 3 generally indicates a cohesive powder that retains air and shows significantly increased resistance at lower blade speeds. Across all batches, the FRI values were marginally above 1, ranging from 1.02 to 1.06, indicating a low sensitivity to changes in flow rate and a generally stable flow behavior. The argon-atomized powder shows marginally lower sensitivity, corresponding to slightly more consistent flow. However, the small difference in FRI values suggests that the two powders have comparable flow characteristics and are both expected to provide stable flow, with a low risk of flow-related issues during powder spreading.

The effect of the morphological features becomes clearer when the apparent density and flow data are considered. Although the argon-atomized powders exhibit slightly higher aspect ratio and circularity, the nitrogen-atomized powders show higher apparent and conditioned bulk densities and lower Hausner ratios (Table 8). This indicates that, within the investigated size range, powder packing and flow are governed less by the small variation in powder sphericity and more by local surface defects such as satellites, which increase particle irregularity, promote interlocking, and increase interparticle friction [63,77]. In this sense, the lower apparent density measured for the argon batches suggests that their slight advantage in overall roundness is at least partially counterbalanced by a stronger satellite-related effect on loose packing. This interpretation is consistent with the present results: the N_2-40 and N_2-45 powders reached apparent densities of 4.30 and 4.33 g/cm^3 and Hausner ratios of 1.05 and 1.06, whereas the Ar-40 and Ar-45 powders showed 4.21 and 4.06 g/cm^3 and 1.13 and 1.15, respectively. The Hall-flow results in Table 9 follow the same trend, confirming that powders with lower interparticle friction flow more readily. Therefore, for the K340 powders investigated here, the slight argon-related advantage in shape regularity does not necessarily translate into superior rheological behavior, because satellite-related effects on packing efficiency and friction are likely more influential than the modest differences captured by aspect ratio and circularity alone.

3.3. Powder density

While the rheological assessment confirmed the favorable dynamic behavior of the feedstock, the internal integrity of the particles is equally critical for the mechanical performance of the final deposited parts. A common challenge in gas atomization is the formation of internal porosity, which typically results from the physical entrapment of the high-pressure gas within the molten droplets during atomization. As reported in the literature, processing parameters, specifically the melt temperature, the atomizing gas type and its pressure, significantly influence the volume fraction of these entrapped gas pores [5]. To quantify the extent of this phenomenon and evaluate the influence of atomizing conditions on material density, the true density of the powders within the 45−125 μm range was measured. The corresponding results are presented in Table 10.

As evidenced by the data, the nitrogen-atomized powders exhibited consistently higher true density values compared to their argon-atomized counterparts within the same particle size range. This observation aligns with similar findings reported in the literature for duplex stainless steel powder [22]. This behavior can be interpreted considering the ability of nitrogen to dissolve in the steel matrix, unlike argon, which is inert and insoluble. Entrapped nitrogen can dissolve into the solidifying matrix, thereby potentially reducing the volume of permanent gas porosity. Additionally, within the investigated processing window, no significant difference was found between the powders atomized with the same gas but at different pressures, indicating that the chemical nature of the gas can be the dominant factor influencing internal porosity. It should be noted, however, that the pressure difference between batches processed with the same atomizing gas in this study was relatively small.

3.4. Chemical composition

To evaluate potential compositional changes induced by the atomization process, the chemical composition of powders within the 45−125 μm size range was analyzed. The quantitative results for the different atomization batches are presented in Table 11. The elemental composition of the atomized powders remains in good agreement with the specifications of the starting rolled K340 scrap. This comparison should be interpreted with caution, as different analytical techniques were used (combustion analysis and OES for the bulk material, SEM/EDS for the powders). Consequently, deviations observed for certain elements, such as Mo, may reflect measurement differences rather than actual compositional changes.

Table 10
Density measurements of the four different powder batches within the particle size range of 45−125 μm.

Batch	Ar – 40 bar	Ar – 45 bar	N_2 – 40 bar	N_2 – 45 bar
True density (g/cm^3)	7.65	7.68	7.75	7.76

Table 11
Chemical composition (wt.%) of the powders produced within the 45−125 μm size range.

Batch	C	Cr	Mo	V	Mn	Si	Al	Nb
Ar – 40 bar	1.07	8.00	1.73	0.44	0.46	0.79	0.81	0.09
Ar – 45 bar	1.07	8.09	1.71	0.44	0.39	0.74	0.73	0.11
N_2 – 40 bar	1.08	8.05	1.67	0.43	0.42	0.82	0.98	0.09
N_2 – 45 bar	1.07	8.13	1.85	0.42	0.44	0.80	0.86	0.10

The concentrations of all major alloying elements fall within the standard tolerance ranges for this steel grade. It should be noted that the aluminum content measured in both the starting material and the atomized powder, although consistent with each other, is slightly higher than the value expected based on the supplier specification [49]. A comparative analysis across the four batches reveals no significant variations, suggesting that variations in atomizing gas type and pressure did not affect the overall chemical stability of the produced powders. While the major alloying elements exhibited a uniform distribution, the contents of the interstitial elements, namely oxygen and nitrogen, required further examination. The compositional analysis performed on the 45–125 μm powder fraction suitable for DED revealed an increase in nitrogen for N_2-atomized powders (0.025 ± 0.003 wt.%) compared to Ar-atomized powders (0.011 ± 0.002 wt.%), and a comparable amount of oxygen (0.007 ± 0.001 and 0.006 ± 0.001 wt.%, respectively). The nitrogen content in the 45–125 μm range is largely influenced by the contribution of larger particles due to the higher volume. Nitrogen is dissolved in solid solution but may also be associated with porosity in larger particles, where this mechanism is more frequent. Similarly, when atomizing with argon, the porosities in large powders are expected to be filled with argon, thus reducing the overall amount of nitrogen being measured. The oxygen content, on the other hand, is dominated by smaller powders, due to the higher specific surface; nevertheless, the difference in oxygen content was not relevant on the 45–125 μm fraction. Therefore, a detailed compositional analysis was carried out on different particle size fractions of the powders atomized at 45 bar. The results illustrated in Fig. 7 revealed that the oxygen and nitrogen content showed distinct variations depending on the particle size range.

The oxygen content shows a clear inverse relationship with particle size, increasing as particle diameter decreases. This trend is associated with the higher surface-to-mass ratio of finer particles. Nevertheless, the absolute oxygen levels remain limited to a few hundred ppm, which is not considered detrimental for AM processing. When comparing the atomizing gases, nitrogen-atomized powders showed slightly lower oxygen contents than argon-atomized powders. Although this difference is within experimental uncertainty, it may be related to differences in cooling rates during powder production, as nitrogen has a higher specific heat capacity and thermal conductivity than argon, promoting faster solidification and a shorter time for oxidation [69]. Given that the variation is close to the inherent experimental uncertainty of the adopted method, the observed difference is likely the combined result of these process-related effects and measurement uncertainty.

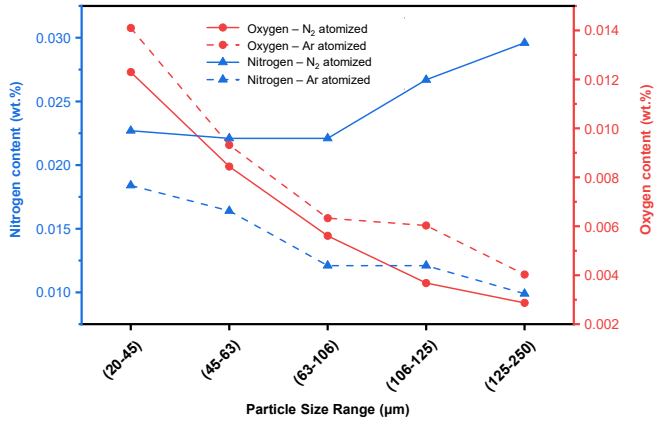


Fig. 7. Graph showing the oxygen and nitrogen content of the particles with different size ranges.

Distinct from the oxygen trends, the nitrogen content showed a complex dependency on both the atomizing gas and the particle size. While the argon-atomized powders displayed a decreasing nitrogen trend with increasing particle size, the nitrogen-atomized batches showed the opposite behavior, with concentrations generally increasing from 0.022 wt.% to 0.030 wt.% as the particles became coarser. Consequently, the gap between the nitrogen-content profiles of argon- and nitrogen-atomized powders widened significantly across the particle size range. Specifically, for the fine particle fraction (20−45 μm), the nitrogen-atomized powder contained approximately 23% more nitrogen content than the argon-atomized powder. In the coarser fractions (125−250 μm), this difference became significantly larger, with the nitrogen-atomized powder exhibiting nearly 200% higher nitrogen content compared to the argon-atomized baseline. This significant uptake aligns with established literature. As reported by Boes et al. [30], the nitrogen content increased from 0.014 wt.% to 0.18 wt.% in nitrogen-atomized martensitic steels, while Janowski et al. [78] observed an increase from 0.025 wt.% to 0.077 wt.% for 304L steel.

The mechanism driving this uptake involves the dissociation of diatomic nitrogen (N_2) and its absorption into the molten steel, limited by solubility [79]. However, the trends differ significantly by gas type. In nitrogen-atomized powders, the higher nitrogen content in coarser fractions can be explained by two main factors: first, the relatively slower cooling of large droplets compared to fine ones extends the time available for nitrogen absorption; second, larger particles contain higher internal porosity, which physically entraps nitrogen gas. Conversely, argon-atomized powders exhibit a declining trend with increasing particle size. Here, the higher nitrogen level in the fine fraction is driven by surface adsorption due to the high surface-to-mass ratio. Since the pores in larger argon-atomized particles entrap inert argon rather than nitrogen, the nitrogen concentration naturally decreases as the surface area contribution diminishes in coarser sizes.

3.5. Solidification structure

The cooling rate is known to play a key role in determining the solidification microstructure, particularly with respect to the potential transition from dendritic to cellular growth. To provide insight into this possibility, the surface morphologies of the atomized powder particles were analyzed, as presented in Fig. 8.

The particle surfaces display a range of solidification morphologies, including radial dendrites, dendrites, and cellular crystals. For the argon-atomized powders, a size-dependent transition is observed. With decreasing particle size, radial dendrites gradually vanish, while dendrites along with cellular crystals become prominent. In the fine particles, the surface is dominated by cellular crystals. This structural evolution is primarily governed by the cooling rate: rapid solidification favors the formation of cellular crystals due to reduced segregation, whereas slower cooling rates lead to microsegregation within the solid phase, resulting in dendrites or radial dendrites. For instance, in the particle size range of 125−250 μm, a clear network of dendritic structure is visible, consisting of primary, secondary, and higher-order arms, alongside the nucleation site on the particle surface. Additionally, primary and secondary dendritic arms remain visible in particles within the 106−125 μm range. However, by further reducing the size, a mix of dendritic and cellular structures can be seen (Fig. 8e), and the cellular structure becomes more dominant for the fine particles (Fig. 8a) due to the higher cooling rates.

A similar trend was observed for the nitrogen-atomized particles; however, the transition from dendritic to cellular structure initiated at a relatively larger particle size. Moreover, within the particle size range of

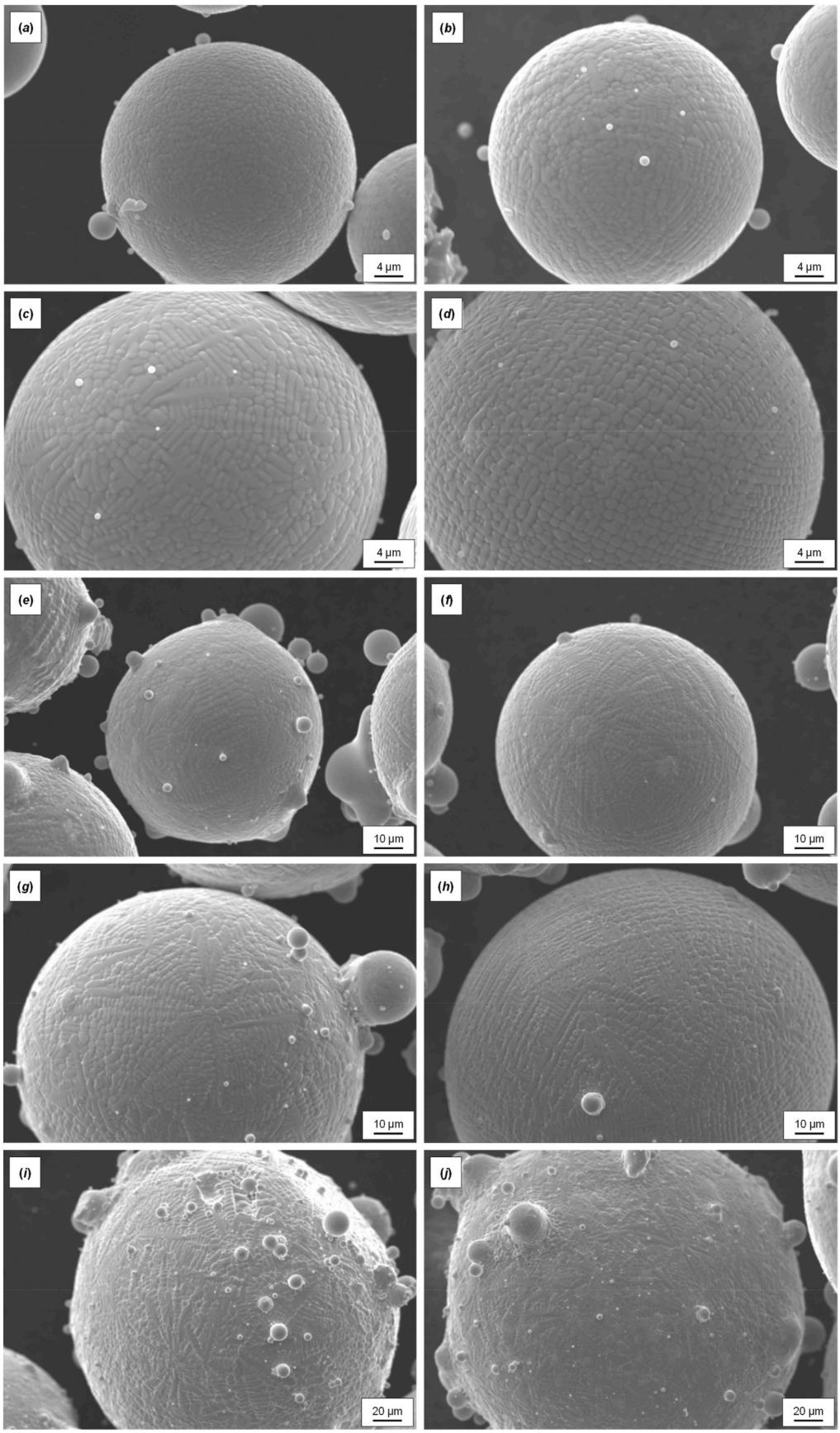


Fig. 8. SEM micrographs of powder particles atomized at 45 bar using argon (left column) and nitrogen (right column) for different particle size ranges: (*a*, *b*) 20−45, (*c*, *d*) 45−63, (*e*, *f*) 63−106, (*g*, *h*) 106−125, and (*i*, *j*) 125−250 μm.

45–63 μm, a higher proportion of cellular structure appears to be present compared to the argon-atomized powder within the same size range. Generally, particles atomized by argon display a more evident dendritic morphology than nitrogen-atomized powders, specifically in the smaller particle sizes, an observation that aligns with findings by Zhong et al. [80]. This difference is attributed to the solidification kinetics; atomization with argon results in a relatively slower solidification rate, as nitrogen possesses a thermal conductivity approximately 1.4 times higher than that of argon [69]. However, the gas properties represent only one variable in the solidification equation; the droplet geometry itself has a major influence on the thermal history. Fundamentally, powder particles of different sizes experience distinct cooling rates. Smaller particles tend to undergo higher cooling rates, leading to a lower grain size [16]. Therefore, determining the cooling rates of the liquid metal during the atomization process is essential for understanding the resulting structure.

3.6. Microstructure, SDAS, and cooling rate

To estimate the cooling rate of the metal during the GA process, theoretical models [81] and experimental techniques based on Secondary Dendrite Arm Spacing (SDAS) measurements [82] are commonly employed. During the solidification phase, dendritic nucleation sites form on the droplet surface. Driven by the anisotropy of the solid-liquid interfacial energy and growth kinetics, these dendrites align with preferred crystallographic orientations and develop secondary dendrite arms. The spacing between these secondary arms is governed by the duration of contact between the solid dendrites and the remaining liquid phase, which is primarily determined by the cooling rate of the powder [83,84]. In the present work, SEM micrographs of particle cross-sections were studied to assess the internal solidification structure (Fig. 9).

It can be seen that the selection of atomizing gas has a considerable effect on the cooling rate of the particles and the resulting microstructure. Consistent with thermophysical principles, nitrogen can provide more efficient heat extraction from the droplets than argon, resulting in a higher effective heat transfer coefficient. Consequently, as quantified in Fig. 10b, for an equivalent particle size, the nitrogen-atomized powders solidify at higher cooling rates and show finer dendritic microstructures (smaller SDAS) compared to their argon-atomized counterparts. For example, based on the regression curves, powder particles with a diameter of ~30 μm produced with nitrogen experienced an estimated cooling rate of ~3.08×10^5 K/s, nearly double that of similar-sized particles atomized with argon under the same pressure (~1.6×10^5 K/s). Correspondingly, the average SDAS in these ~30 μm nitrogen-atomized particles was ~1.05 μm, slightly finer than the ~1.16 μm measured in the argon-atomized particles of comparable size, indicating more rapid solidification kinetics in nitrogen atmosphere.

This enhanced heat extraction capability of nitrogen remains effective across the coarser particle size fractions as well. As indicated in Fig. 10, for the 106–125 μm range (average ~115 μm), the estimated cooling rate for the nitrogen-atomized particles was ~2.14×10^4 K/s compared to ~1.21×10^4 K/s for the argon-atomized particles. Consequently, the nitrogen-atomized powder yielded a finer SDAS of 1.82 μm in contrast to the 2.25 μm measured for the argon counterpart. This trend intensifies in the largest analyzed fraction (125–250 μm, average ~187.5 μm), where nitrogen provided a significantly higher cooling rate (~9.8×10^3 K/s) than argon (~3.6×10^3 K/s), resulting in a correspondingly finer dendritic spacing (SDAS of ~2.47 μm for the nitrogen-atomized powder relative to 3.37 μm for the argon-atomized powder). These comparisons indicate that, under the same operating conditions,

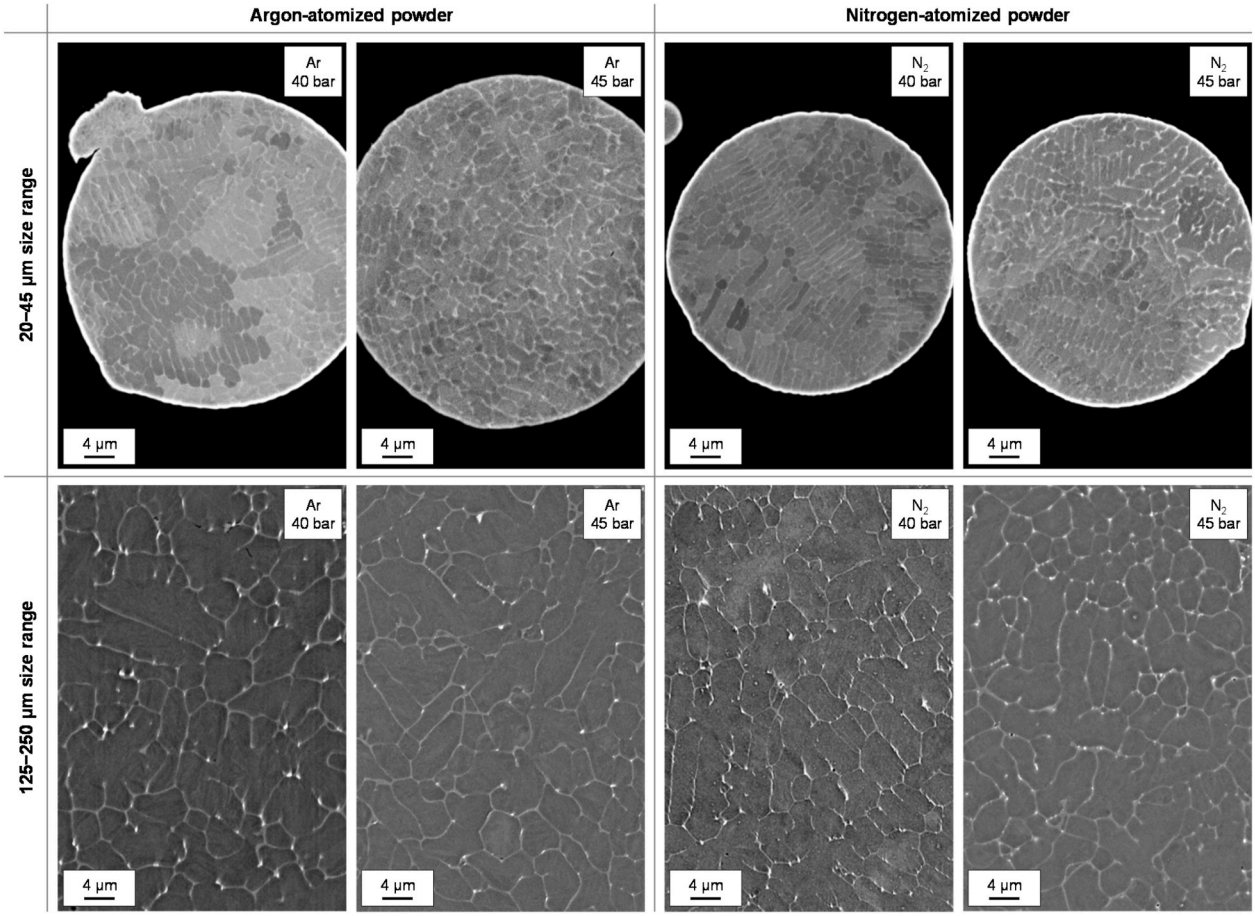


Fig. 9. Cross-sectional micrographs of powder particles in the particle size ranges of 20–45 μm and 125–250 μm, as a function of the atomizing pressure.

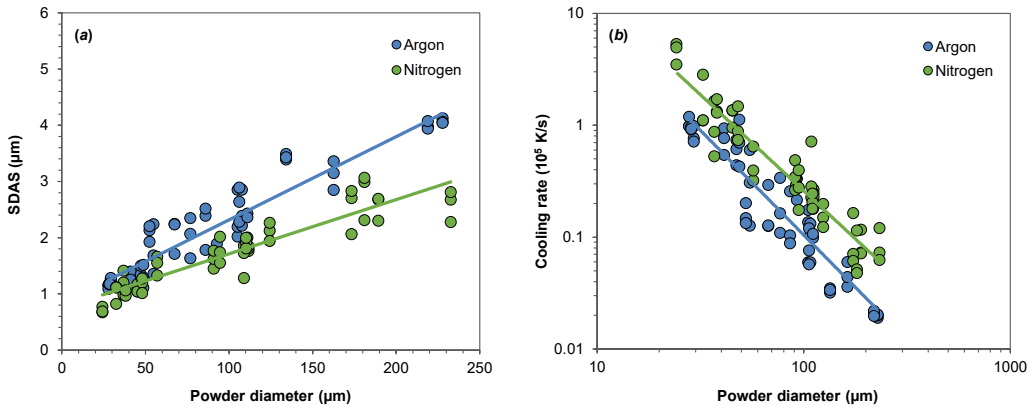


Fig. 10. (*a*) Secondary dendrite arm spacing as a function of particle size measured experimentally, and (*b*) cooling rates calculated from the experimental data for powders produced at an atomizing pressure of 45 bar.

nitrogen tends to promote faster solidification and enhanced microstructural refinement than argon. Notably, these experimental results align with the numerical simulations reported by Shi et al. [85] regarding the gas atomization of a high-vanadium steel with a carbon content comparable to K340, using both argon and nitrogen.

3.7. XRD analysis

In this work, XRD was employed to characterize the phase constitution and crystallographic structure of the atomized powders. When analyzing powders with different particle size ranges, XRD provides valuable insights into crystallite sizes and lattice strains. Assuming that different production batches follow a similar trend in peak characteristics as a function of particle size, XRD analysis was conducted on six particle size ranges of the argon-atomized powder. The resulting diffraction patterns are shown in Fig. 11.

The results indicate that the microstructure of the particles is predominantly characterized by austenite. While microsegregation of alloying elements was previously observed in the solidification morphology, the bulk phase constitution remains largely austenitic across the majority of the size distributions. However, it should be noted that in the very fine particles (<20 μm), an additional peak corresponding to BCC iron is evident. This observation is attributed to the extremely high cooling rates experienced by these droplets. Under such rapid solidification conditions, the austenite may transform into martensite (a BCC/BCT phase) or δ-ferrite, resulting in the observed extra peak. To better understand the effect of particle size and cooling rate on these structural parameters, detailed information obtained from the XRD analysis is provided in Table 12.

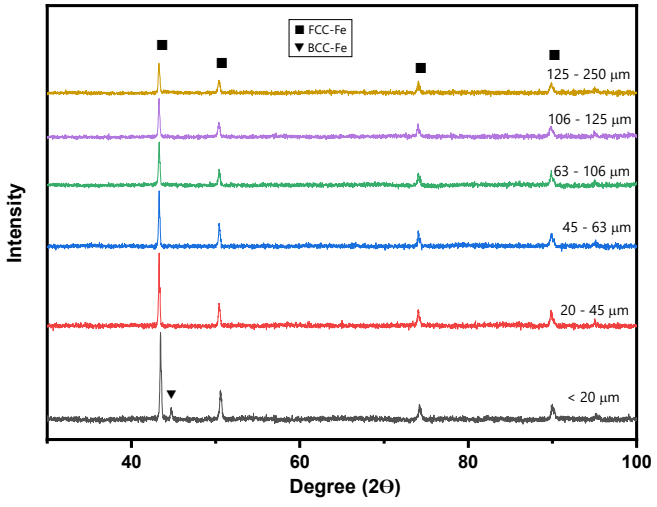


Fig. 11. XRD patterns of argon-atomized powders for different particle size ranges, produced at an atomizing pressure of 40 bar.

In XRD analysis, peak positions are governed by Bragg's law, relating the diffraction angle (2θ) to the interplanar spacing (*d*) and the X-ray wavelength (λ_x). A shift toward higher 2θ values indicates a decrease in d-spacing due to lattice contraction, whereas a shift toward lower 2θ values corresponds to an increase in d-spacing associated with lattice expansion. Additionally, peak broadening may occur due to variations in crystallite size and the presence of microstrain effects. Based on the quantitative results summarized in Table 12, as particle size increases, peak positions shift slightly to lower diffraction angles, which may be associated with marginally larger d-spacings. As an example, the d-spacing of Peak 1 increases from 2.08 Å for the <20 μm fraction to 2.09 Å for the 125−250 μm fraction. This trend indicates minor fluctuations in lattice parameters, potentially arising from variations in residual stresses or slight compositional differences among the particle size fractions. This variation is likely driven by the different thermal histories experienced by the droplets. Smaller powder particles often experience higher surface-induced stresses during rapid solidification. These compressive stresses contract the crystal lattice, resulting in smaller d-spacings and, consequently, higher 2θ values. Conversely, larger particles tend to exhibit more relaxed lattices (i.e., reduced surface-induced

Table 12
Parameters extracted from XRD analysis for powder particles in different size ranges. The peak located at 44.7°, observed only in particles smaller than 20 μm, was excluded from the comparison.

Particle size range	Peak no.	<20 μm	45–63 μm	125–250 μm
Position (°)	Peak 1	43.44	43.27	43.25
	Peak 2	50.56	50.41	50.36
	Peak 3	74.19	74.07	74.04
	Peak 4	89.95	89.85	89.81
	Peak 5	95.18	95.02	95.02
FWHM (°)	Peak 1	0.12	0.12	0.15
	Peak 2	0.20	0.15	0.22
	Peak 3	0.19	0.16	0.18
	Peak 4	0.33	0.29	0.33
	Peak 5	0.70	0.50	0.31
d-spacing (Å)	Peak 1	2.08	2.09	2.09
	Peak 2	1.80	1.81	1.81
	Peak 3	1.28	1.28	1.28
	Peak 4	1.09	1.09	1.09
	Peak 5	1.04	1.04	1.05
Microstrain (%)	Peak 1	0.018	0.065	0.090
	Peak 2	0.070	0.072	0.096
	Peak 3	0.004	0.041	0.028
	Peak 4	0.132	0.088	0.136
	Peak 5	0.287	0.211	0.084

stresses), resulting in slightly increased d-spacing and a shift of peaks toward lower 2θ values.

Complementary to the analysis of peak positions, the examination of peak broadening, specifically the Full Width at Half Maximum (FWHM), provides information on the microstructural refinement and lattice defect density. Generally, peak broadening is governed by two primary factors: crystallite size and lattice microstrain. According to the Scherrer equation, a reduction in average crystallite size correlates directly with broader diffraction peaks [86]. Additionally, lattice imperfections such as dislocations, defects, and inhomogeneous strain fields contribute to this broadening. Typically, smaller particles exhibit higher microstrain due to the high density of defects introduced during rapid cooling. However, larger particles are not immune to these effects and may develop residual strain arising from differential cooling gradients. In the present dataset (Table 12), the measured FWHM values vary with particle size, yet no consistent monotonic trend is evident across all analyzed peaks. This irregularity suggests that each crystallographic plane responds differently to internal stresses and strain. Consequently, the lack of a uniform trend implies that, unlike the lattice parameter changes observed in the peak positions, the crystallite size and microstrain do not vary systematically with particle size in this specific material system.

Further analysis of the calculated microstrain values indicates that these internal lattice distortions can also contribute to the observed peak shifts. Microstrain values were estimated from the XRD peak broadening using the Williamson-Hall approach. The total broadening of each diffraction peak was assumed to arise from the combined contribution of finite crystallite size and lattice strain after Eq. (4):

$$\beta \cos\theta = \frac{k\lambda_x}{D} + 4\varepsilon \sin\theta \tag{4}$$

where β is the Full Width at Half Maximum (FWHM) of the diffraction peak, corrected for instrumental broadening and expressed in radians; θ is the Bragg angle; k is the dimensionless shape factor (typically assumed equal to 0.9); λ_x is the wavelength of the incident X-ray radiation; D is the apparent crystallite size; and ε is the lattice microstrain, representing the distribution of local lattice distortions within the material. Accordingly, the corrected full width at half maximum, β, expressed in radians, was related to the Bragg angle, θ. The FWHM values extracted from the fitted diffraction peaks were first converted from degrees to radians and corrected for instrumental broadening. The microstrain was then obtained from the slope of the linear fit of $\beta\cos\theta$ as a function of $4\sin\theta$. The calculated values were used as comparative indicators of lattice distortion among the different powder size fractions. Consistent with the variations in peak broadening, the microstrain shows a complex dependence on both particle size and crystallographic orientation. While some diffraction peaks suggest elevated microstrain in the finer fractions, others indicate higher microstrain levels in the coarser particles, confirming that the stress state is not uniform across all lattice planes. Theoretically, the high surface-to-volume ratio of smaller particles facilitates rapid heat extraction, trapping defects and dislocations that increase microstrain. Conversely, larger particles experience slower cooling, which typically allows for lattice relaxation and a reduction in residual stresses. However, the experimental results demonstrate that local inhomogeneities can still induce significant strain accumulation in specific planes within the larger particles, potentially overriding the general trend of stress relief.

3.8. Carbon footprint results

Consistent with the defined goal and scope, system boundaries, and key assumptions described in Section 2.2, the carbon footprint assessment was based on a combination of primary and secondary data sources. Laboratory-scale experimental measurements constituted the main source of primary data, while secondary datasets were used where direct measurements were not available, particularly for modelling upstream material production. Secondary data were primarily obtained from the Granta Selector 2025 R1 database (version 25.1.2, Ansys Inc.) and complemented with values reported in the literature. To account for parameter uncertainty, value ranges and sensitivity analyses were introduced when deemed appropriate. The following Sections 3.8.1 and 3.8.2 present the results of the life cycle inventory (LCI) and the corresponding carbon footprint contributions for the different material input scenarios and atomization conditions (discussed in Section 3.8.3).

3.8.1. Carbon footprint of feedstock materials

As defined in Section 2.2, bulky industrial scrap derived from rolled K340 steel was employed as feedstock for gas atomization. In accordance with the 100:0 recycled content approach, no upstream burdens associated with raw material extraction and alloy production were allocated to the scrap, which was modelled as pre-consumer recycled material [60]. To quantify the potential carbon footprint reduction associated with direct scrap atomization, two reference scenarios were additionally assumed: the use of virgin-grade and typical-grade K340 alloy. For these scenarios, upstream environmental impacts related to primary raw material extraction and metallurgical processing were included and are collectively referred to as 'material production' (see Fig. 3). Given the lack of data specific to K340 steel in the literature or in the selected database, LCI datasets for another tool steel, AISI H13, were adopted as a proxy for modelling upstream material production impacts [87]. This choice was motivated by the comparable alloy class, similar alloying system, and analogous industrial processing routes. Accordingly, the carbon footprint associated with upstream material production was assumed as 5.2 ± 0.3 $kgCO_2$/kg for virgin-grade material and 3.7 ± 0.2 $kgCO_2$/kg for typical-grade material.

To assess the suitability of H13 steel as a proxy for K340, an independent consistency check was performed in accordance with the approach proposed by Ehmsen et al. [88]. A composition-based environmental impact indicator (EI) was calculated for K340 by multiplying the nominal elemental mass fractions by the corresponding characterization factors obtained from the Granta Selector database, as listed in Table 13. The EI represents a composition-based indicator specifically intended to capture the contribution of alloy chemistry to environmental impacts, without explicitly resolving process-specific metallurgical steps. In the present study, it is therefore used as a complementary tool to support proxy selection rather than as a stand-alone estimate of the carbon footprint. Within this scope, the resulting EI values for K340 were 5.5 ± 0.3 $kgCO_2$/kg for virgin-grade material and 4.4 ± 0.2 $kgCO_2$/kg for typical-grade material. Although slightly higher, the close agreement between the resulting EI values and those of the proxy material supports the use of H13-based datasets as a reasonable proxy for K340.

With the upstream material baseline established, the assessment further accounted for the impacts associated with 'feedstock production' for the virgin-grade and typical-grade scenarios (Fig. 3). Feedstock production refers to the pre-manufacturing operations required to obtain commercial semi-finished products suitable for the process (e.g., rolled bars). For this stage, a yield of 0.95 and a carbon footprint of 3.0 ± 0.2 $kgCO_2$ per kg of semi-finished output were adopted, in accordance with data from the Granta Selector database. For the scrap scenario, the mass flow entering the atomization stage corresponds to the experimentally measured charged mass of 6.4 ± 0.1 kg per atomization run (m_{load}). For the virgin-grade and typical-grade benchmark scenarios, the same charged mass was assumed for comparability; therefore, the corresponding upstream raw material input (m_{raw}) was estimated to be approximately 6.8 ± 0.1 kg per atomization run, when a yield factor of 0.995 for feedstock/scrap preparation is considered [61].

3.8.2. Carbon footprint of gas atomization

Beyond the contribution of feedstock materials, the carbon footprint of gas atomization includes process-related emissions associated with

Table 13
Composition-based data used for the calculation of the environmental impact indicator (EI) of K340 alloy. Elements reported as additions in the database (i.e., Al and Nb) were excluded from the EI calculation.

Element	wt.%	Virgin grade CF ($kgCO_2$/kg element)	Typical grade CF ($kgCO_2$/kg element)
C (carbon)	1.1	0.3 ± 0.1	0.3 ± 0.1
Si (silicon)	0.9	11.4 ± 0.6	11.4 ± 0.6
Mn (manganese)	0.4	4.9 ± 0.2	3.7 ± 0.2
Cr (chromium)	8.3	21.7 ± 1.1	20.7 ± 1.0
Mo (molybdenum)	2.1	17.2 ± 0.8	15.1 ± 0.7
V (vanadium)	0.5	242.0 ± 12.0	176.0 ± 9.0
Fe (iron), balance	86.7	2.3 ± 0.1	1.6 ± 0.1
Total EI ($kgCO_2$/kg alloy)		5.5 ± 0.3	4.4 ± 0.2

melting and atomization, as well as auxiliary operations such as feedstock or scrap preparation and powder sieving. For this purpose, primary data were collected at the laboratory scale, reflecting the specific experimental configuration investigated in this study. Electrical energy demand was monitored using a Schneider PM 3250 power analyzer, while atomizing gas consumption was measured using a Platon GMTX flowmeter installed on the high-pressure gas line. The electricity requirements were converted into CO_2 emissions using a greenhouse gas emission intensity of 0.19 $kgCO_2$/kWh, corresponding to the 2024 average value for the EU-27 area [89]. Moreover, since electricity represents a significant contribution to the gate-to-gate impacts of GA, a range of emission intensities from 0.05 to 0.50 $kgCO_2$/kWh was considered to reflect geographical differences and operational variability in electricity supply, spanning highly decarbonized power systems to more carbon-intensive electricity mixes. In addition, each electricity scenario was further perturbed by ± 10% to represent short-term grid fluctuations and uncertainties associated with emission-factor determination.

The powder production process begins with the preparation of the metal charge prior to its introduction into the melting chamber. The 'scrap preparation' (Fig. 3) consisted of (*i*) cutting the material into smaller pieces suitable for loading into the atomizer crucible, followed by (*ii*) ultrasonic cleaning. As identical feedstock masses were processed across all atomization batches (6.4 ± 0.1 kg), the electrical energy demand associated with band sawing was constant, amounting to 1.5 ± 0.2 kWh per batch, with negligible contributions from tool wear of the cutting blades. The energy and material requirements of the ultrasonic cleaning stage were quantified following the same experimental setup and operating conditions previously reported by Gobber et al. [52], resulting in an energy consumption of 0.06 ± 0.01 kWh per batch and a solvent usage of 0.5 kg per batch, associated with a carbon footprint of 2.0 ± 0.6 $kgCO_2$/kg of solvent. For consistency in the comparative assessment, the energy and consumables demand for feedstock preparation in the virgin-grade and typical-grade scenarios were assumed to be equivalent to those measured for scrap preparation.

The gas atomization process, including the contributions of the induction furnace, vacuum pump, and chiller, required an average electrical energy input of 32.9 ± 0.3 kWh per cycle, with no significant differences observed among the batches. The atomization process resulted in an average material loss of approximately 2%, primarily due to the retention of fine particles within the exhaust filters and the atomization chamber. When considering only the useable powder fraction in the 45–125 μm size range, the resulting net process yield (defined as the ratio of collected powder mass to the initial charged mass) was found to depend on both the atomizing gas type and the applied pressure (Table 3), with direct implications for the carbon footprint results presented in Section 3.8.3. Powder fractions smaller than 45 μm, together with coarse debris larger than 125 μm, are collected in a powder stock and may be reused as feedstock in subsequent atomization cycles.

The impact associated with atomizing gas consumption was evaluated using primary data provided by the industrial gas supplier, accounting for gas production, storage, and transportation to the laboratory. On this basis, carbon footprint factors of 0.18 ± 0.02 $kgCO_2$/kg for argon and 0.24 ± 0.03 $kgCO_2$/kg for nitrogen were adopted [51,52]. It is worth noting that significant discrepancies exist in literature, as other studies relied on alternative data sources (e.g., Ref. [35]), leading to different carbon footprint estimates. These differences highlight the strong case sensitivity of gas-related LCA results and can ultimately lead to contrasting conclusions when comparing the environmental performance of different atomizing gas strategies. Table 14 summarizes the average gas consumption and the corresponding CO_2 emissions per atomization cycle for the different gas types and pressure conditions investigated in this study. The observed dependence of gas consumption on atomizing gas type and pressure is primarily related to changes in the atomization regime and process efficiency (as discussed in Section 3.2) which influence both the duration of atomization and the effective gas flow required to achieve the target powder size distribution, and consequently the associated CO_2 emissions.

Moreover, refractories and consumables employed during the atomization process also contribute to the overall carbon footprint of the produced powders. The consumables considered in this study (including the crucible, stopper rod, crucible insert, melt delivery tube, and melt delivery nozzle) together with their constituent materials and number of uses prior to replacement, were identical to those reported in Table 7 of Ref. [52]. The carbon footprint of primary production of high-purity (typical-grade) alumina was assumed to be 2.8 ± 0.1 $kgCO_2$/kg, in accordance with data from the Granta Selector database. Similarly, boron nitride was assigned a carbon footprint of 6.8 ± 0.4 $kgCO_2$/kg. On this basis, the total contribution of refractories and consumables to carbon emissions was estimated to be 3.30 ± 0.12 $kgCO_2$ per batch. Finally, the specific energy consumption of the sieving stage was taken as 0.18 ± 0.02 kWh per kg of input powder.

3.8.3. *Carbon footprint of powder production*

Given the LCI dataset, when the carbon footprint is evaluated on a per-batch basis (independently of the resulting powder size distribution) the results show that variations in atomization conditions have a limited effect on the total emissions. For the virgin-grade input material scenario, assuming a greenhouse gas emission intensity for electricity production of 0.19 ± 0.02 $kgCO_2$/kWh, total values range from 67.3 ± 4.0 $kgCO_2$/batch (Ar – 40 bar) to 67.7 ± 4.1 $kgCO_2$/batch (N_2 – 45 bar), corresponding to variations below 1%. Similar trends are observed for the typical-grade scenario, where total emissions vary from 57.1 ± 3.5 to 57.6 ± 3.6 $kgCO_2$/batch, and for the scrap scenario, where values range from 12.8 ± 1.5 to 13.2 ± 1.6 $kgCO_2$/batch across the different gas-type and pressure combinations. This weak sensitivity arises from

Table 14
Average consumption of atomizing gases and associated CO_2 emissions per atomization batch.

Batch	Ar – 40 bar	Ar – 45 bar	N_2 – 40 bar	N_2 – 45 bar
Gas consumption (kg/batch)	9.5 ± 0.5	9.4 ± 0.5	7.5 ± 0.4	9.0 ± 0.4
CO_2 emissions ($kgCO_2$/batch)	1.71 ± 0.29	1.69 ± 0.29	1.80 ± 0.33	2.16 ± 0.38

the relative weight of the different contributions: emissions are largely dominated by material-related stages (for the virgin- and typical-grade scenarios) and by the electrical energy demand of gas atomization, which was experimentally quantified in 32.9 ± 0.3 kWh per cycle, with no significant differences among batches. Although measurable differences exist in atomizing-gas consumption and in the adopted gas-specific emission factors, the contribution of the gas itself remains relatively modest in absolute terms (Table 14) and therefore does not substantially affect the batch-level carbon footprint.

In contrast, when the batch-level values are normalized to 1 kg of useable powder in the 45–125 μm size range, which represents the relevant functional unit for DED applications, the carbon footprint results (in Fig. 12) become directly linked to variations in process yield within the target PSD range. Under argon, the yield of the 45–125 μm fraction increases from 50.8% to 54.6% as the atomization pressure is raised from 40 to 45 bar, whereas under nitrogen it decreases from 43.3% to 41.8% over the same pressure interval (see Table 3). These yield differences result in different specific impacts per kilogram of powder. Consequently, the environmental performance of different atomization strategies cannot be assessed solely on the basis of gas-specific emission factors, but must account for their combined effect on gas consumption, process efficiency, and powder yield. While the present analysis is subject to limitations related to laboratory-scale operation and the adopted modeling assumptions, the observed distribution of impact contributions is in line with previous cradle-to-gate assessments of gas-atomized powders. In particular, Priarone et al. [61] reported that, for industrial AISI 316L powder production, approximately 85% of the total carbon footprint per kilogram of useable powder is attributable to input materials when typical-grade supply is considered, while the powder production stage accounts for the remaining ~15%.

The dominant contribution of upstream material sourcing relative to powder manufacturing highlights the effectiveness of using scrap as a feedstock for the decarbonization of metal powder production. When the results are expressed per kilogram of useable powder in the 45–125 μm size range, the use of scrap as atomization feedstock leads to a substantial reduction in carbon footprint of up to approximately 77–78% (on average) with respect to the typical-grade scenario and 80–81% relative to the virgin-grade material scenario. From a strictly environmental perspective, this decarbonization strategy appears particularly relevant for high-impact alloy systems. In this context, Benedetti et al. [50] similarly reported that producing Inconel 718 powder from bulky scrap can reduce both the carbon footprint and the energy demand by more than 90% compared with conventional production routes, supporting the general validity of the trends observed in the present study.

Fig. 13 presents the results of the sensitivity analysis performed by varying the greenhouse gas emission intensity of electricity generation between 0.05 and 0.50 $kgCO_2$/kWh, while considering different feedstock material scenarios and atomization conditions. The analysis is limited to the LCI framework defined in Section 3.8.2 and affects all powder production contributions directly linked to electricity consumption, including gas atomization as the dominant term, as well as, to a lesser extent, feedstock/scrap preparation and powder sieving. In contrast, the impacts associated with consumables (atomizing gases and refractories) and with upstream material sourcing were kept constant across the sensitivity analysis. As expected, the carbon footprint per kilogram of useable powder exhibits a linear dependence on the electricity emission factor for all scenarios. The slope of this dependence is similar for argon and nitrogen under otherwise identical conditions, whereas the values differ markedly between the virgin-, typical-, and scrap-based feedstock scenarios. These results confirm that, although the carbon intensity of electricity generation is a relevant parameter for powder production, upstream material sourcing remains a dominant driver of the overall carbon footprint, in agreement with previous findings [61].

Although the DED process was not experimentally performed in the present study, a literature-based estimate was included to provide a broader perspective on the environmental implications of using scrap feedstock. The electrical energy demand and argon consumption of the DED process were derived from the work of Gouveia et al. [90] and taken as 37.3 kWh and 5.7 kg of argon, respectively, per kilogram of deposited powder, using H13 steel as the reference material, consistent with the assumptions adopted for the upstream stages. By applying the corresponding conversion factors of 0.19 ± 0.02 $kgCO_2$/kWh for electricity and 0.18 ± 0.02 $kgCO_2$/kg for argon, the DED stage results in an estimated carbon footprint of 8.1 ± 0.9 $kgCO_2$ per kilogram of deposited material. When this value is compared with the carbon footprint of powder production, it can be observed that, when virgin- or typical-grade feedstock is used, the upstream powder production stage remains the dominant contributor to the overall environmental impact. In contrast, when powder is produced from recycled scrap and modelled using the 100:0 recycled content approach, the contribution of powder production is substantially reduced, and the relative weight of the downstream DED process becomes comparable or even dominant. This evidence underscores that the relative environmental relevance of powder production and part manufacturing is largely influenced by the

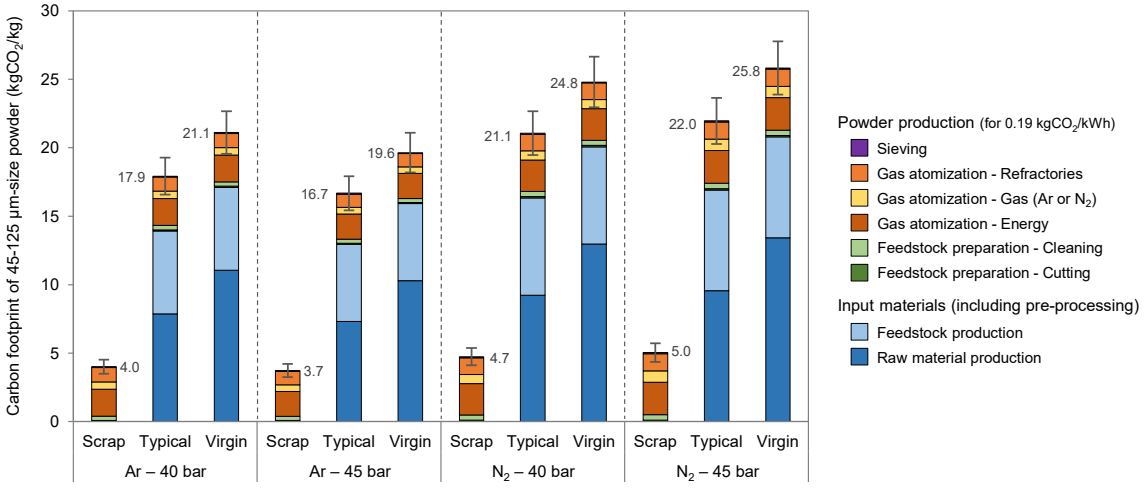


Fig. 12. Carbon footprint of 45-125 μm-size powder as a function of atomization conditions, expressed per kg of useable powder, assuming a greenhouse gas emission intensity for electricity production of 0.19 ± 0.02 $kgCO_2$/kWh.

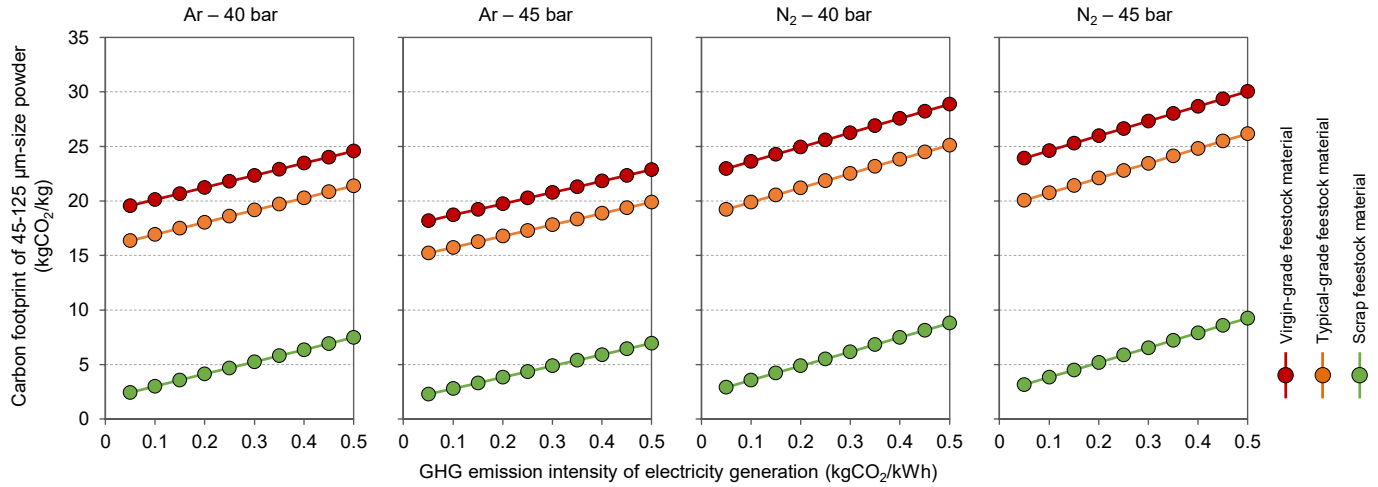


Fig. 13. Sensitivity of the carbon footprint of 45–125 μm-size powder (average values) to the GHG emission intensity of electricity generation.

adopted feedstock strategy [61], and that the benefits of scrap-based powder production extend beyond the powder stage by alleviating the environmental burden associated with upstream material sourcing [51].

4. Conclusions and outlook

This study demonstrates the feasibility of producing K340 tool steel powder via vacuum induction melting inert gas atomization (VIGA) and systematically evaluates the influence of atomizing gas (argon and nitrogen) and gas pressure (40 and 45 bar) on powder characteristics and environmental performance. The main results are summarized in Table 15. The DED-suitable 45–125 μm fraction ranged from 41.8 to 54.6 wt.%, corresponding to a 12.8 percentage-point span, with the main variation associated with the type of atomizing gas. Increasing pressure reduced median particle size under argon, whereas under nitrogen it led to larger particles, which is attributed to the formation of a partially solidified layer at the nozzle that altered gas-melt interaction. When averaged across the two pressure levels, nitrogen atomization led to an increase in apparent density from 4.14 to 4.32 g/cm^3 (+4.4%) and in conditioned bulk density from 4.38 to 4.58 g/cm^3 (+4.5%). In parallel, the Hausner ratio decreased from 1.14 to 1.06 (−7.0%) relative to argon. The same trend was observed at the individual pressure levels, with the most pronounced differences observed at 45 bar, where nitrogen increased both apparent and conditioned bulk density by about 6.7% compared with argon. From a metallurgical standpoint, the powders remained consistent with the starting K340 chemistry, although nitrogen atomization caused a measurable nitrogen pickup of 0.03 wt.%, particularly in the coarser fraction.

When assessed from a cradle-to-gate environmental perspective, the carbon footprint per atomization batch showed limited sensitivity to gas type and pressure, as batch-level emissions were dominated by upstream material-related contributions and electrical energy consumption. In contrast, when results were normalized to 1 kg of useable powder in the 45–125 μm size range, significant differences emerged due to variations in process yield. The use of recycled scrap as atomization feedstock, modelled according to a 100:0 recycled content approach, led to substantial reductions in carbon footprint, up to approximately 77–78% relative to typical-grade material and 80–81% relative to virgin-grade material. Sensitivity analysis to electricity carbon intensity indicated that, although electricity significantly influences absolute values, upstream material sourcing remains the dominant driver of environmental impact when virgin or typical feedstocks are used. Although supplier-specific primary data indicate a slightly higher carbon footprint per kilogram for nitrogen compared to argon, the contribution of atomizing gas remains limited in absolute terms. Consequently, even if alternative emission factors were adopted, the overall ranking between feedstock scenarios and the main conclusions of this study would not be significantly affected. The present study is subject to some limitations. The powder production as well as the environmental assessment were performed at laboratory scale. Upstream material production for K340 was modelled using H13 as a proxy; while suitable for comparative purposes, absolute values should be interpreted with caution. Despite these

Table 15
Summary of the main powder characteristics and environmental performance as a function of atomizing gas type and pressure. Note: SDAS and cooling rate values are derived from measurements on representative particle sizes and are not differentiated by atomizing pressure.

Parameter	Ar – 40 bar	Ar – 45 bar	N_2 – 40 bar	N_2 – 45 bar	Main trends
Yield, 45–125 μm fraction (wt.%)	50.8	54.6	43.3	41.8	Lower with N_2; increases with pressure (Ar), decreases with pressure (N_2)
D50 (μm)	93	81	112	118	Higher with N_2; decreases with pressure (Ar), increases with pressure (N_2)
SDAS, ~30 μm particle size (μm)	1.16	–	1.05	–	Finer with N_2
SDAS, ~115 μm particle size (μm)	2.25	–	1.82	–	Finer with N_2
Cooling rate, ~30 μm (K/s)	1.60×10^5	–	3.08×10^5	–	Higher with N_2
Cooling rate, ~115 μm (K/s)	1.21×10^4	–	2.14×10^4	–	
Apparent density (g/cm^3)	4.21	4.06	4.30	4.33	Higher with N_2; weak dependence on pressure
Conditioned bulk density (g/cm^3)	4.45	4.31	4.55	4.60	
Hausner ratio (−)	1.13	1.15	1.05	1.06	Lower with N_2; weak dependence on pressure
Hall flowability (s)	15.7	16.4	14.2	14.5	Faster flow with N_2
Nitrogen content, 45–125 μm fraction (wt. %)	0.011	–	0.025	–	Higher with N_2; varies with particle size
CF, virgin-grade feedstock ($kgCO_2$/kg)	19.5–22.7	18.1–21.1	23.0–26.6	23.9–27.7	Higher with N_2 (due to lower yield); strongly dependent on feedstock
CF, scrap feedstock ($kgCO_2$/kg)	3.5–4.5	3.2–4.3	4.1–5.3	4.3–5.7	

limitations, the consistency of the trends observed (both internally and with previous cradle-to-gate assessments of metal powder production) supports the robustness of the main findings.

Declaration of competing interest

The authors declare that they have no known competing financial interests or personal relationships that could have appeared to influence the work reported in this paper.

Acknowledgements

The authors would like to thank Giorgio Zanolla for the preparation of metallographic samples and the laboratory staff of the Alessandria Campus of Politecnico di Torino (Enrico Pallavicini and Dario Pezzini) for their support during the experimental activities.

References

[1] DebRoy T, Wei HL, Zuback JS, Mukherjee T, Elmer JW, Milewski JO, et al. Additive manufacturing of metallic components – process, structure and properties. Prog Mater Sci 2018;92:112–224. https://doi.org/10.1016/j.pmatsci.2017.10.001.

[2] Kenevisi MS, Yu Y, Lin F. A review on additive manufacturing of Al–Cu (2xxx) aluminium alloys, processes and defects. Mater Sci Tech-Lond 2021;37(9):805–29. https://doi.org/10.1080/02670836.2021.1958487.

[3] Kassym K, Perveen A. Atomization processes of metal powders for 3D printing. Mater Today Proc 2020;26(2):1727–33. https://doi.org/10.1016/j.matpr.2020.02.364.

[4] Anderson IE, White EMH, Dehoff R. Feedstock powder processing research needs for additive manufacturing development. Curr Opin Solid State Mater Sci 2018;22(1):8–15. https://doi.org/10.1016/j.cossms.2018.01.002.

[5] Kenevisi MS, Lin F. Effect of powder characteristics on relative density and porosity formation during electron beam selective melting of Al2024 aluminum alloy. J Manuf Sci Eng 2023;145(5):054501. https://doi.org/10.1115/1.4056665.

[6] Beckers D, Ellendt N, Fritsching U, Uhlenwinkel V. Impact of process flow conditions on particle morphology in metal powder production via gas atomization. Adv Powder Technol 2020;31(1):300–11. https://doi.org/10.1016/j.apt.2019.10.022.

[7] Gao CF, Xiao ZY, Zou HP, Liu ZQ, Chen J, Li SK, et al. Characterization of spherical AlSi10Mg powder produced by double-nozzle gas atomization using different parameters. Trans Nonferrous Met Soc China (English Edition) 2019;29(2):374–84. https://doi.org/10.1016/S1003-6326(19)64947-2.

[8] Li XG, Zhu Q, Shu S, Fan JZ, Zhang. SM Fine spherical powder production during gas atomization of pressurized melts through melt nozzles with a small inner diameter. Powder Technol 2019;356:759–68. https://doi.org/10.1016/j.powtec.2019.09.023.

[9] Mullis AM, Farrell L, Cochrane RF, Adkins NJ. Estimation of cooling rates during close-coupled gas atomization using secondary dendrite arm spacing measurement. Metall Mater Trans B 2013;44:992–9. https://doi.org/10.1007/s11663-013-9856-2.

[10] Mathias LET, Andreoli AF, Gargarella P. Gas atomization of A2 tool steel: effect of process parameters on powders' physical properties. J Alloys Compd 2023;960:170696. https://doi.org/10.1016/j.jallcom.2023.170696.

[11] Ni G, Wang S, Li Q, Zhao D, Song C, Li C. Preparation of Cr17Mn11Mo3N powders by high-pressure gas atomization and the nitrogen increasing mechanism. Powder Technol 2021;385:490–500. https://doi.org/10.1016/j.powtec.2021.03.025.

[12] Wang P, Li J, Wang X, Du BR, Shen SY, Ge XY, et al. Impact mechanism of gas temperature in metal powder production via gas atomization. Chin Phys B 2021;30(5):054702. https://doi.org/10.1088/1674-1056/abd75e.

[13] Wu J, Xia M, Wang J, Ge CC. Effect of electrode induction melting gas atomization process on fine powder yields: continuous metal melt flow. Arch Metall Mater 2023;68(3):839–49. https://doi.org/10.24425/amm.2023.145446.

[14] Chen G, Tan P, Zhao SY, He WW, Tang HP. Spherical Ti-6Al-4V powders produced by gas atomization. Key Eng Mater 2016;704:287–92. https://dx.doi.org/10.4028/www.scientific.net/KEM.704.287.

[15] Martín A, Cepeda-Jiménez CM, Pérez-Prado MT. Gas atomization of γ-TiAl alloy powder for additive manufacturing. Adv Eng Mater 2020;22(1):1900594. https://doi.org/10.1002/adem.201900594.

[16] Sarriegui G, Martín JM, Burgos N, Ipatov M, Zhukov AP, Gonzalez J. Effect of particle size on grain growth of Nd-Fe-B powders produced by gas atomization. Mater Charact 2022;187:111824. https://doi.org/10.1016/j.matchar.2022.111824.

[17] Lv X, Liu Z, Lei T, Li Q, Zhao F, Peng K, et al. Microstructure and properties of cu-cr-nb alloy powder prepared by argon gas atomization. Adv Powder Technol 2019;30(11):2464–72. https://doi.org/10.1016/j.apt.2019.07.013.

[18] Fedina T, Sundqvist J, Powell J, Kaplan AFH. A comparative study of water and gas atomized low alloy steel powders for additive manufacturing. Addit Manuf 2020;36:101675. https://doi.org/10.1016/j.addma.2020.101675.

[19] Neikov OD, Naboychenko SS, Murashova IB, editors. Handbook of non-ferrous metal powders: technologies and applications. Oxford: Elsevier; 2009.

[20] Cai C, Zhou K. Metal additive manufacturing. In: Patel CD, Chen CH, editors. Digital manufacturing: the industrialization of art to part 3D additive printing. Oxford: Elsevier; 2022. p. 247–98. https://doi.org/10.1016/B978-0-323-95062-6.00005-X.

[21] Lawley A. Atomization. In: Buschow KHJ, Cahn RW, Flemings MC, editors. Encyclopedia of materials: science and technology. Oxford: Elsevier; 2001. p. 387–92.

[22] Cui C, Stern F, Ellendt N, Uhlenwinkel V, Steinbacher M, Tenkamp J, et al. Gas atomization of duplex stainless steel powder for laser powder bed fusion. Materials 2023;16(1):435. https://doi.org/10.3390/ma16010435.

[23] Singh D, Dangwal S. Effects of process parameters on surface morphology of metal powders produced by free fall gas atomization. J Mater Sci 2006;41:3853–60. https://doi.org/10.1007/s10853-006-6652-2.

[24] Ouyang HW, Chen X, Huang BY. Influence of melt superheat on breakup process of close-coupled gas atomization. Trans Nonferrous Met Soc China (English Edition) 2007;17(5):967–73. https://doi.org/10.1016/S1003-6326(07)60209-X.

[25] Lagutkin S, Achelis L, Sheikhaliev S, Uhlenwinkel V, Srivastava V. Atomization process for metal powder. Mater Sci Eng A 2004;383(1):1–6. https://doi.org/10.1016/j.msea.2004.02.059.

[26] Cui B, Chen K, Yang Y, Lv Y, Zhang F, Liu S. Effect of ultrasonic vibration on the pores and properties of the laser-arc hybrid welding joint of high nitrogen steel. Mater Chem Phys 2024;318:129297. https://doi.org/10.1016/j.matchemphys.2024.129297.

[27] Li G, Shi G, Miao H, Liu D, Li Z, Wang M, et al. Effects of the gas-atomization pressure and annealing temperature on the microstructure and performance of FeSiBCuNb nanocrystalline soft magnetic composites. Materials 2023;16(3):1284. https://doi.org/10.3390/ma16031284.

[28] Gerling R, Leitgeb R, Schimansky FP. Porosity and argon concentration in gas atomized γ-TiAl powder and hot isostatically pressed compacts. Mater Sci Eng A 1998;252(2):239–47. https://doi.org/10.1016/S0921-5093(98)00656-X.

[29] Sun L, Liu Y, Li J, Chen K, Gao Y, Yang G. Morphology and microstructure of Fe–Cr–W–B alloy powders prepared by argon gas atomization. Vacuum 2022;200:111046. https://doi.org/10.1016/j.vacuum.2022.111046.

[30] Boes J, Röttger A, Theisen W, Cui C, Uhlenwinkel V, Schulz A, et al. Gas atomization and laser additive manufacturing of nitrogen-alloyed martensitic stainless steel. Addit Manuf 2020;34:101379. https://doi.org/10.1016/j.addma.2020.101379.

[31] Dong H, Chai G, Guo X. High nitrogen steels. Steel Res Int 2023;94(10):2300505. https://doi.org/10.1002/srin.202300505.

[32] Heikkilä I. The positive effect of nitrogen alloying of tool steels used in sheet forming [PhD thesis]. Uppsala University; 2013. https://www.diva-portal.org/smash/get/diva2:617657/FULLTEXT01.pdf.

[33] Adin MŞ. Machining aerospace aluminium alloy with cryo-treated and untreated HSS cutting tools. Adv Mater Process Te 2024;10(3):2664–89. https://doi.org/10.1080/2374068X.2023.2273035.

[34] Koç S, Adin MŞ, İlenç R, Bronis M, Ekinci S. Sound-based tool wear classification in turning of AISI 316L using multidomain acoustic features and SHAP-enhanced gradient boosting models. Materials 2026;19(5):861. https://doi.org/10.3390/ma19050861.

[35] Ehmsen S, Conrads J, Klar M, Aurich JC. Environmental impact of powder production for additive manufacturing: carbon footprint and cumulative energy demand of gas atomization. J Manuf Syst 2025;82:13–25. https://doi.org/10.1016/j.jmsy.2025.05.004.

[36] Hara R, Yamamoto M, Ito G, Kamimiyada K, Narita I, Miyahara H. Effect of nitrogen on the microstructure and hardness of high-carbon high-speed tool steel type alloys. Mater Trans 2016;57(11):1945–51. https://doi.org/10.2320/matertrans.M2016124.

[37] Boccalini M, Goldenstein H. Solidification of high speed steels. Int Mater Rev 2001;46(2):92–115. https://doi.org/10.1179/095066001101528411.

[38] Lefor K, Walter M, Weddeling A, Hryha E, Huth S, Weber S, et al. Influence of the PM-processing route and nitrogen content on the properties of Ni-free austenitic stainless steel. Metall Mater Trans A 2015;46:1154–67. https://doi.org/10.1007/s11661-014-2701-7.

[39] Mattar T, Ibrahim KM, Fathy A, El Faramawy H. Improving the wear resistance of M41 steel by nitrogen alloying and ESR. Mater Charact 2007;58(5):407–15. https://doi.org/10.1016/j.matchar.2006.06.007.

[40] Cieśla M, Ducki KJ. Influence of increased nitrogen content on tool steels structure and selected properties. J Achiev Mater Manuf Eng 2008;27(2):123–6.

[41] Luo YW, Guo HJ, Sun XL, Guo J. Influence of the nitrogen content on the carbide transformation of AISI M42 high-speed steels during annealing. Sci Rep 2018;8:4328. https://doi.org/10.1038/s41598-018-22461-z.

[42] Choi S, Kim H, Sung J, Lee D, Seo J. Properties of tool steels printed by directed energy deposition process on S45C base metal. Materials 2020;13(22):5068. https://doi.org/10.3390/ma13225068.

[43] Gill SS, Singh J, Singh R, Singh H. Metallurgical principles of cryogenically treated tool steels - a review on the current state of science. Int J Adv Manuf Technol 2010;54:59–82. https://doi.org/10.1007/s00170-010-2935-5.

[44] Rahito Wahab DA, Azman AH. Additive manufacturing for repair and restoration in remanufacturing: an overview from object design and systems perspectives. Processes 2019;7(11):802. https://doi.org/10.3390/pr7110802.

[45] Kanishka K, Acherjee B. A systematic review of additive manufacturing-based remanufacturing techniques for component repair and restoration. J Manuf Process 2023;89:220–83. https://doi.org/10.1016/j.jmapro.2023.01.034.

[46] Li L, Zhang X, Pan T, Liou F. Component repair using additive manufacturing: experiments and thermal modeling. Int J Adv Manuf Technol 2022;119:719–32. https://doi.org/10.1007/s00170-021-08265-y.

[47] Aprilia A, Wu N, Zhou W. Repair and restoration of engineering components by laser directed energy deposition. Mater Today Proc 2022;70:206–11. https://doi.org/10.1016/j.matpr.2022.09.022.
[48] Jovičević-Klug P, Tóth L, Podgornik B. Comparison of K340 steel microstructure and mechanical properties using shallow and deep cryogenic treatment. Coatings 2022;12(9):1296. https://doi.org/10.3390/coatings12091296.
[49] Voestalpine BÖHLER Edelstahl GmbH & Co. Cold work tool steel BÖHLER K340 n. d. www.voestalpine.com/bohler-edelstahl.
[50] Benedetti M, Perini M, Vanazzi M, Giorgini A, Macoretta G, Menapace C. Atomized scrap powder feedstock for sustainable inconel 718 additive manufacturing via LPBF: a study of static and fatigue properties. Progr Addit Manuf 2024;9:1843–56. https://doi.org/10.1007/s40964-023-00547-z.
[51] Monti C, Gobber FS, Turani M, Papis K, Priarone PC, Actis Grande M, et al. Evaluating the use of scrap metal to produce Al-5Cu-3Ti-1Cr-1Fe alloy powder for laser powder bed fusion. Sustain Mater Technol 2025;45:e01606. https://doi.org/10.1016/j.susmat.2025.e01606.
[52] Gobber FS, Priarone PC, Pennacchio A, Actis Grande M. Effect of inert gas pressure on the properties and carbon footprint of UNS S32760 powders made from waste materials by gas atomization. J Mater Res Technol 2024;33:8814–28. https://doi.org/10.1016/j.jmrt.2024.11.195.
[53] ASTM B213-20. Standard test methods for flow rate of metal powders using the hall flowmeter funnel. West Conshohocken, PA: ASTM International; 2020.
[54] Airoldi L, Brucculeri R, Baldini P, Morganti S, Grande MA, Gobber FS, et al. Coupling direct powder deposition with spark plasma sintering: a new approach towards rapid prototyping. Progr Addit Manuf 2024;9:1953–66. https://doi.org/10.1007/s40964-023-00552-2.
[55] Jegede OE, Haque N, Mullis AM, Cochrane RF. Relationship between cooling rate and SDAS in liquid phase separated metastable Cu–Co alloys. J Alloys Compd 2021;883:160823. https://doi.org/10.1016/j.jallcom.2021.160823.
[56] Mao M, Guo H, Wang F, Sun X. Effect of cooling rate on the solidification microstructure and characteristics of primary carbides in H13 steel. ISIJ Int 2019;59(5):848–57. https://doi.org/10.2355/isijinternational.ISIJINT-2018-524.
[57] ISO 14040:2006. Environmental management - life cycle assessment - principles and framework. 2006. Published, Edition 2, https://www.iso.org/standard/37456.html.
[58] ISO 14044:2006. Environmental management - life cycle assessment - requirements and guidelines. 2006. Published, Edition 1, https://www.iso.org/standard/38498.html.
[59] ISO 14067:2018. Greenhouse gases - carbon footprint of products - requirements and guidelines for quantification. 2018. Published, Edition 1, https://www.iso.org/standard/71206.html.
[60] Zampori L, Pant R. Suggestions for updating the product environmental footprint (PEF) method. EUR 29682 EN. Luxembourg: Publications Office of the European Union; 2019. https://doi.org/10.2760/424613. https://publications.jrc.ec.europa.eu/repository/handle/JRC115959.
[61] Priarone PC, Gobber FS, Cacace S. Parametric modeling of cradle-to-gate carbon emissions from gas-atomized AISI 316L powders under closed-loop feedstock strategies. Powder Technol 2026;470:121949. https://doi.org/10.1016/j.powtec.2025.121949.
[62] Gao MZ, Ludwig B, Palmer TA. Impact of atomization gas on characteristics of austenitic stainless steel powder feedstocks for additive manufacturing. Powder Technol 2021;383:30–42. https://doi.org/10.1016/j.powtec.2020.12.005.
[63] Zhang LC, Xu WY, Li Z, Zheng L, Liu YF, Zhang GQ. Mechanism of rapidly solidified satellites formation in gas atomized powders: simulation and characterization. Powder Technol 2023;418:118162. https://doi.org/10.1016/j.powtec.2022.118162.
[64] Li Z, Mukai K, Zeze M, Mills KC. Determination of the surface tension of liquid stainless steel. J Mater Sci 2005;40:2191–5. https://doi.org/10.1007/s10853-005-1931-x.
[65] Sharan A, Nagasaka T, Cramb AW. Surface tensions of liquid Fe-Cr and Fe-Cr-N alloys. Metall Mater Trans B 1994;25:626–8. https://doi.org/10.1007/BF02650084.
[66] Shi Y, Lu W, Sun W, Zhang S, Yang B, Wang J. Impact of gas pressure on particle feature in Fe-based amorphous alloy powders via gas atomization: simulation and experiment. J Mater Sci Technol 2022;105:203–13. https://doi.org/10.1016/j.jmst.2021.06.075.
[67] Qing Y, Guo K, Liu C, Qin Y, Zhan Y, Shuo S, et al. Impact of atomization pressure on the particle size of nickel-based superalloy powders by numerical simulation. Materials 2022;15(9):3020. https://doi.org/10.3390/ma15093020.
[68] Aydin O, Unal R. Experimental and numerical modeling of the gas atomization nozzle for gas flow behavior. Comput Fluids 2011;42(1):37–43. https://doi.org/10.1016/j.compfluid.2010.10.013.
[69] Fang P, Xu Y, Li X, Chen Y. Influence of atomizing gas and cooling rate on solidification characterization of nickel-based superalloy powders. Rare Met Mater Eng 2018;47(2):423–30. https://doi.org/10.1016/s1875-5372(18)30082-1.
[70] Elsayed MMA. Microstructural characterization of carrier-based dry powder inhalation excipients: insights and guidance. Int J Pharm 2019;568:118482. https://doi.org/10.1016/j.ijpharm.2019.118482.
[71] Fitzpatrick J. Powder properties in food production systems. In: Bhandari B, Bansal N, Zhang M, Schuck P, editors. Handbook of food powders: chemistry and technology. second ed. Oxford: Elsevier; 2023. p. 203–18. https://doi.org/10.1016/B978-0-323-98820-9.00071-5.
[72] Hao T. Understanding empirical powder flowability criteria scaled by hausner ratio or carr index with the analogous viscosity concept. RSC Adv 2015;5:57212–5. https://doi.org/10.1039/c5ra07197f.
[73] Xu G, Lu P, Li M, Liang C, Xu P, Liu D, et al. Investigation on characterization of powder flowability using different testing methods. Exp Therm Fluid Sci 2018;92:390–401. https://doi.org/10.1016/j.expthermflusci.2017.11.008.
[74] Koynov S. Using statistical methods to optimize powder flow measurements and to predict powder processing performance. New Brunswick, NJ: Rutgers University; 2015 [PhD thesis], https://rucore.libraries.rutgers.edu/rutgers-lib/47459/.
[75] Li T, Wang Y, Glasser B, Muzzio F. Predicting feeder performance during hopper refill based on material flow properties. In: Particle technology forum 2017 - core programming area at the 2017 AIChE annual meeting. Minneapolis, MN: AIChE; 2017. p. 169–80.
[76] Brubaker J, Moghtadernejad S. A comprehensive review of the rheological properties of powders in pharmaceuticals. Powders 2024;3(2):233–54. https://doi.org/10.3390/powders3020015.
[77] Wu J, Xia M, Wang J, Zhao B, Ge C. Effect of electrode induction melting gas atomization on powder quality: satellite formation mechanism and pressure. Materials 2023;16(6):2499. https://doi.org/10.3390/ma16062499.
[78] Janowski GM, Biancaniello FS, Ridder SD. Beneficial effects of nitrogen atomization on an austenitic stainless steel. Metall Trans A 1992;23(1):3263–72. https://doi.org/10.1007/bf03024533.
[79] Feichtinger HK, Stein G. Melting of high nitrogen steels. Mater Sci Forum 1999;318:261–70. https://dx.doi.org/10.4028/www.scientific.net/msf.318-320.261.
[80] Zhong W, Peng H, Jiao D, Qiu W, Liu Z, Xu W, et al. Comparative study of nickel-based super-alloy powders atomized by argon and nitrogen. Powder Metall Met Ceram 2023;61:633–43. https://doi.org/10.1007/s11106-023-00352-x.
[81] Wang Y, Huang S, Wang B, Zhou J, Chen C. Numerical study on heat transfer, deformation, and breakup of flying droplets during gas atomization of molten aluminum. Metals 2026;16(1):37. https://doi.org/10.3390/met16010037.
[82] Gianoglio D, Ciftci N, Armstrong S, Uhlenwinkel V, Battezzati L. On the cooling rate-microstructure relationship in molten metal gas atomization. Metall Mater Trans A 2021;52:3750–8. https://doi.org/10.1007/s11661-021-06325-2.
[83] Lavernia EJ, Srivatsan TS. The rapid solidification processing of materials: science, principles, technology, advances, and applications. J Mater Sci 2010;45:287–325. https://doi.org/10.1007/s10853-009-3995-5.
[84] Reiter AE, Derflinger VH, Hanselmann B, Bachmann T, Sartory B. Investigation of the properties of $Al_{1-x}CrxN$ coatings prepared by cathodic arc evaporation. Surf Coat Technol 2005;200(7):2114–22. https://doi.org/10.1016/j.surfcoat.2005.01.043.
[85] Shi Y, Li X, Wang P, Liang Y, Ge C. Impact of atomizing medium on the characteristics of high-vanadium steel powder: a comparative study of nitrogen and argon. J Mater Res Technol 2025;35:4660–76. https://doi.org/10.1016/j.jmrt.2025.02.087.
[86] Albers P. Catalyst characterization. In: Cornils B, Herrmann WA, Muhler M, Wong CH, editors. Catalysis from A to Z: a concise encyclopedia. fourth ed. Weinheim: Wiley-VCH; 2013. p. 416–8. https://doi.org/10.1002/9783527671380.
[87] Ashby MF. Materials and the environment. third ed. Woburn, MA: Elsevier; 2021. https://doi.org/10.1016/C2016-0-04008-1.
[88] Ehmsen S, Klar M, Aurich JC. Evaluating the environmental impact of additive manufacturing: a methodology to determine the environmental impact of parts manufactured by high-speed laser directed energy deposition. Proced CIRP 2024;122:91–6. https://doi.org/10.1016/j.procir.2024.01.013.
[89] European Environment Agency (EEA). Greenhouse gas emission intensity of electricity generation, country level. https://www.eea.europa.eu/en/analysis/indicators/greenhouse-gas-emission-intensity-of-1. [Accessed 30 April 2026].
[90] Gouveia JR, Pinto SM, Campos S, Matos JR, Sobral J, Esteves S, et al. Life cycle assessment and cost analysis of additive manufacturing repair processes in the mold industry. Sustainability 2022;14(4):2105. https://doi.org/10.3390/su14042105.